ASO-based *PKM* Splice-switching Therapy Inhibits Hepatocellular Carcinoma Cell Growth

Wai Kit Ma[1], Juergen Scharner[1,2], Ana S. H. Costa[1], Hyun Yun Jeong[1,2], Michaela Jackson[3], Frank Rigo[3], C. Frank Bennett[3], Adrian R. Krainer[1]

1 Cold Spring Harbor Laboratory, Cold Spring Harbor, NY
2 Current addresss: Stoke Therapeutics, Bedford, MA
3 Ionis Pharmaceuticals, Carlsbad, CA

Correspondence should be addressed to A.R.K. (krainer@cshl.edu)
Cold Spring Harbor, NY 11724
Phone: 516-367-8417
Fax: 516-367-8453
Email: krainer@cshl.edu

The work was performed at Cold Spring Harbor Laboratory, Cold Spring Harbor, NY, USA

Running title: *PKM* Antisense Therapy for Liver Cancer

Keywords: Antisense oligonucleotide; ASO; pyruvate kinase; PKM; hepatocellular carcinoma

Abstract

The M2 pyruvate kinase (PKM2) isoform is upregulated in most cancers and plays a crucial role in the Warburg effect, which is characterized by the preference for aerobic glycolysis for energy metabolism. PKM2 is an alternative-splice isoform of the *PKM* gene, and is a potential therapeutic target. Previously, we developed antisense oligonucleotides (ASOs) that switch *PKM* splicing from the cancer-associated *PKM2* to the *PKM1* isoform and induce apoptosis in cultured glioblastoma cells. Here, we explore the potential of ASO-based *PKM* splice-switching as a targeted therapy for liver cancer. We utilize a lead cEt/DNA ASO, which has a higher potency than MOE modification, to demonstrate that it induces *PKM* splice-switching and inhibits the growth of cultured hepatocellular-carcinoma (HCC) cells. This *PKM* isoform switch increases pyruvate-kinase activity and alters glucose metabolism. The lead ASO inhibits tumorigenesis in an orthotopic-xenograft HCC mouse model. Finally, a surrogate mouse-specific ASO induces *Pkm* splice-switching and inhibits HCC growth, without observable toxicity, in a genetic HCC mouse model.

Statement of significance

Antisense oligonucleotides are used to force a change in *PKM* isoform usage in HCC, reversing the Warburg effect and inhibiting tumorigenesis.

Introduction

Liver cancer is the second leading cause of cancer death worldwide, and its mortality rate continues to rise (1). The World Health Organization estimates that there will be more than 1 million deaths from liver cancer annually by 2030. Liver cancer has very poor prognosis, with an 18.1% 5-year survival rate in the US (2). Hepatocellular carcinoma (HCC) accounts for 90% of all the primary liver-cancer cases (3). Curative therapies, including resection, liver transplantation, and local ablation, are only applicable to patients with early-stage HCC. However, early detection remains challenging. Chemoembolization treatment is suitable for patients with intermediate-stage HCC, but it carries a risk of non-target embolization, with numerous side effects. Systemic therapies, including four kinase inhibitors, an antibody against VEGF, and an immune-checkpoint inhibitor, are available for patients with advanced-stage HCC. However, the improvements in patient outcomes remain modest (4,5). Thus, new therapies need to be developed to address the major unmet needs in HCC management.

Reprogramming of energy metabolism is a hallmark of cancer. Cancer cells fulfill the rapid cell-growth requirement by altering their metabolism to increase the generation of building blocks for macromolecule biosynthesis. This metabolic rewiring can be achieved by decreasing the catalytic activity of pyruvate kinase at one of the rate-limiting steps of glycolysis: the conversion of phosphoenolpyruvate to pyruvate (6,7). There are four isoforms of pyruvate kinase (PKL, PKR, PKM1, and PKM2), which are encoded by *PKLR* and *PKM* genes in mammals. *PKLR* encodes PKL and PKR, each of which is expressed from a tissue-specific promoter (8). PKL is primarily expressed in liver and kidney, whereas PKR is highly expressed in red blood cells. PKM1 and PKM2 are derived from the *PKM* gene, which consists of 12 exons, of which exons 9 and 10 are mutually exclusive: PKM1 includes exon 9 but not exon 10, whereas PKM2 includes exon 10 but not exon 9 (9). *PKM1* is expressed in terminally differentiated, non-proliferating cells, whereas *PKM2* is highly expressed in proliferating embryonic cells and many types of cancer (10–12). Among all four pyruvate kinase isoforms, PKM1 is the only constitutively active isoform, whereas the other three isoforms are allosterically regulated by fructose-1,6-biphosphate (FBP) (13,14). Furthermore, binding of phosphorylated tyrosine proteins to the allosteric pocket. and post-translational modification can both suppress PKM2 enzymatic activity (15–18). Given that the reduced enzymatic activity of PKM2 is crucial to provide a metabolic advantage for tumorigenesis (17), several small molecules have been developed to activate PKM2 as a strategy to treat cancer (19–21). Numerous studies demonstrated that PKM2 activators can inhibit cancer-cell growth (22,23). In an alternative strategy, down-

regulation of *PKM2* induces apoptosis of cancer cells, both *in vivo* and *in vitro* (24–26), suggesting that PKM2 is a potential therapeutic target. Furthermore, PKM1 was shown to have tumor-suppressor activity (27). Replacement of PKM2 with PKM1 in cancer cells inhibited cell proliferation and delayed tumor formation in nude-mouse xenografts (12), suggesting that simultaneously downregulating PKM2 while upregulating PKM1 in cancer cells could be an especially effective strategy to treat cancer.

ASOs are powerful therapeutic tools that function by binding specific RNA-target sequences via Watson-Crick base pairing. Targeting RNA with ASOs is used in a diverse range of applications, including degradation of RNA, alteration of RNA splicing, inhibition of RNA translation, modification of RNA structure, and disruption of the interaction between RNA-binding proteins and RNA (28). Different chemical modifications in the phosphate backbone, ribose sugar, and nucleobase are used to determine the precise mechanism of action or to enhance the pharmacological properties of ASOs (29). We previously developed antisense oligonucleotides (ASOs) to switch *PKM* splicing from *PKM2* to *PKM1* in cultured glioblastoma and HEK293 cells (30). This isoform switch causes cultured glioblastoma cells to undergo apoptosis in a dose-dependent manner (30), suggesting the potential of these ASOs for cancer therapy**.**

Systemically delivered ASOs preferentially accumulate in the liver (31). This makes the liver a preferred target organ for ASO splice-switching therapy. In this study, we investigated the efficacy of ASO-based *PKM* splice-switching as a targeted therapy for liver cancer, using cell-culture and mouse models. We show that a lead ASO inhibits the growth of cultured HCC by increasing the *PKM1* to *PKM2* ratio. We also demonstrate that ASO1-cEt/DNA enhances pyruvate kinase activity and diverts glucose carbons from anabolic processes to oxidative phosphorylation in the tricarboxylic-acid (TCA) cycle in cultured HCC. Moreover, we observed that ASO1-cEt/DNA delays liver-tumor formation in a xenograft mouse model. We also identified a mouse-specific ASO that promotes *mPKM* splice-switching and inhibits HCC growth in a genetic HCC mouse model. In summary, we demonstrate the efficacy of ASO-based *PKM* splicing-switching therapy in different pre-clinical models, suggesting its clinical potential for the treatment of liver cancer.

Results

ASO1-cEt/DNA switches *PKM* splicing in HCC cells

PKL is the predominant pyruvate kinase isoform expressed in normal liver (8). However, PKM2 is overexpressed in numerous types of cancer, including liver cancer (11,32,33). We compared *PKL* and *PKM2* transcript levels between HCC cell lines and normal adult liver by RT-qPCR. We found that both HepG2 and Huh7 cells express less than half *PKLR* mRNA levels, but ≥12-fold higher *PKM* mRNA levels than normal adult liver (Supplementary Fig. 1). This analysis suggests that the ASO therapeutic target, PKM2, is the predominant isoform in HCC cells, which is consistent with a previous study (32).

We previously developed a 15-mer ASO with uniform 2'-O-methoxyethyl (MOE) modifications that can switch *PKM* splicing in HEK293 and glioblastoma cells (30). Here, we asked whether we can similarly switch *PKM* splicing in HCC cells. Given that ASOs with 2', 4'-constrained 2'-O-ethyl and DNA mixed-chemistry (cEt/DNA) can have higher potency than ASOs with MOE modifications (34), we re-designed the PKM-ASO with cEt/DNA modification. In addition, we increased the length of the ASO to 18-mer, to further increase the specificity and affinity toward the *PKM2* target. We identified ASO1-cEt/DNA as the most potent ASO for *PKM* switching in HCC cells using an ASO single-nucleotide "microwalk" along the previously identified *PKM*-targeting region ((30); data not shown). To show that ASO1-cEt/DNA induces *PKM* splice-switching, we transfected 60 nM ASO1-cEt/DNA or Ctrl-cEt/DNA into HCC cells and analyzed *PKM* RNA splicing by radioactive RT-PCR. ASO1-cEt/DNA increased the *PKM1* isoform and decreased the *PKM2* isoform (Fig. 1A and Supplementary Fig. 1B). *PKM1* mRNA levels increased ~16-fold and ~10-fold in Huh7 and HepG2 cells, respectively (Fig. 1B and Supplementary Fig. 1C). *PKM* splice-switching was specific to ASO1-cEt/DNA, as no splice-switching was observed upon Ctrl-cEt/DNA treatment. Skipping of both exon 9 and exon 10 in *PKM* RNA produces the *PKMds* isoform, which harbors a premature termination codon on exon 11, such that *PKMds* mRNA is destabilized by nonsense-mediated decay (35). Consistent with our previous study (30), we detected *PKMds* isoform in both HCC cell lines upon ASO1-cEt/DNA treatment (Fig. 1A, Fig. 1B, Supplementary Fig. 1B and Supplementary Fig. 1C).

We further verified *PKM* splice-switching upon ASO1-cEt/DNA treatment by RT-qPCR. ASO1-cEt/DNA simultaneously increased *PKM1* mRNA and decreased *PKM2* mRNA, but the total *PKM* transcript level remained unchanged in both HCC cell lines (Fig. 1C, Supplementary Fig. 1D). Consistent with the RNA measurements, *PKM* splice-switching led to an increase in PKM1 and a decrease in PKM2 protein levels in Huh7 cells (Fig. 1D). However, in HepG2 cells, we only observed an increase in PKM1 protein, but no significant change in PKM2 and total

PKM protein levels (Supplementary Fig. 1E). A potential explanation for this apparent discrepancy in HepG2 cells could be a longer half-life of PKM2 and/or selection against cells with lower PKM2 levels. Nevertheless, our data indicate that transfection of ASO1-cEt/DNA induces *PKM* splice-switching.

Because transfection does not accurately recapitulate *in vivo* delivery of ASO, we next asked whether ASO1-cEt/DNA can induce *PKM* splice-switching in the absence of any delivery reagents (free uptake). HCC cells were treated with varying concentrations of ASO1-cEt/DNA by free uptake prior to radioactive RT-PCR. Although *PKM* splice-switching induced by ASO1-cEt/DNA via free uptake was less potent than by transfection, we observed significant *PKM* splice-switching in both HepG2 and Huh7 cells in a dose-dependent manner after four days of treatment (Fig. 2A, Fig. 2B, Supplementary Fig. 1F, Supplementary Fig. 1G). Interestingly, *PKM1* levels increased to 8% in Huh7 cells and 10% in HepG2 cells when extending the treatment period to seven days at 20 μM ASO1-cEt/DNA (Fig. 2A – Fig. 2D, Supplementary Fig. 1F - Supplementary Fig. 1I). Furthermore, we observed *PKM* splice-switching at the protein level in Huh7 cells (Fig 2E). Consistent with the transfection results, we observed increased PKM1 protein level but no significant reduction in PKM2 protein level in HepG2 cells, upon ASO1-cEt/DNA treatment (Supplementary Fig. 1J). We conclude that ASO1-cEt/DNA induces *PKM* splice-switching in HCC cells, although in one of the cell lines the reduction in PKM2 is less apparent due to its stability or to negative selection (see below).

ASO1-cEt/DNA inhibits HCC cell growth

Next, we asked whether ASO-mediated *PKM* splice-switching affects HCC cells *in vitro*. Upon ASO1-cEt/DNA treatment by free uptake, we observed several changes, including cell elongation and reduced cell density, in both Huh7 and HepG2 cells, suggesting potential cell toxicity and/or reduced proliferation (Supplementary Fig. 2A). Therefore, we asked whether ASO1-cEt/DNA delivered via free uptake affects HCC cell growth. We found significantly slower cell growth of both Huh7 and HepG2 cells by day 5 upon ASO1-cEt/DNA, but not Ctrl-cEt/DNA treatment, consistent with a sequence-specific effect (Fig. 3A, Supplementary Fig. 2B). Next, we investigated whether ASO1-cEt/DNA promotes apoptosis and/or inhibits cellular proliferation. Annexin V staining showed that the proportion of early apoptotic cells increased ~5-fold and ~2-fold upon ASO1-cEt/DNA treatment in Huh7 and HepG2 cells, respectively (Fig. 3B, Fig .3C, Supplementary Fig. 2C, Supplementary Fig. 2D). This result indicates that ASO1-cEt/DNA enhances apoptosis in HCC cells. We then performed EdU staining to determine the effect of ASO1-cEt/DNA on cellular proliferation. We detected a significant decrease in the

percentage of EdU-positive Huh7 and HepG2 cells upon ASO1-cEt/DNA, but not Ctrl-cEt/DNA treatment (Fig. 3D, Fig. 3E, Supplementary Fig. 2E, Supplementary Fig. 2F), indicating that ASO1-cEt/DNA inhibits the proliferation of HCC cells. In conclusion, ASO1-cEt/DNA induces apoptosis and inhibits cellular proliferation, slowing down HCC cell growth.

The ASO1-cEt/DNA-dependent slow-growth phenotype is an on-target effect

Next, we tested whether the ASO1-cEt/DNA-dependent slow-growth phenotype is caused by *PKM* splice-switching from PKM2 to PKM1. We generated HCC cells that stably express T7-PKM2 cDNA and analyzed their growth (Supplementary Fig. 3). To determine whether T7-PKM2 is catalytically active, we assayed pyruvate kinase enzymatic activity in HCC cells expressing T7-PKM2 or luciferase-strawberry, with or without 5 mM FBP. There was no significant difference in pyruvate kinase activity between cells expressing T7-PKM2 and luciferase-strawberry in the absence of FBP (Supplementary Fig. 3C). However, cells expressing T7-PKM2 had ~3-fold higher pyruvate kinase activity than cells expressing luciferase-strawberry in the presence of 5 mM FBP (Supplementary Fig. 3C), indicating that T7-PKM2 is catalytically active in both Huh7 and HepG2 cells. We then tested whether T7-PKM2 can rescue the slow growth caused by ASO1-cEt/DNA. Consistent with the ASO1-cEt/DNA treatment in Huh7 and HepG2 parent cells (Fig. 3A, Supplementary Fig. 2B), ASO1-cEt/DNA suppressed the growth of Huh7 and HepG2 cells that stably expressed luciferase-strawberry (Fig. 4A, Supplementary Fig. 4A). Compared to the cells expressing luciferase-strawberry, enforced expression of T7-PKM2 partially rescued the ASO1-cEt/DNA-dependent slow-growth effect (Fig. 4A, Supplementary Fig. 4A). The slow growth could only be partially rescued, most likely because ASO1-cEt/DNA simultaneously decreased PKM2 and increased PKM1. In contrast, enforced expression of T7-PKM2 restored the PKM2 level, but not PKM1. We conclude that the ASO1-cEt/DNA-dependent slow-growth phenotype is an on-target effect.

We also tested whether expression of T7-PKM2 can rescue ASO1-cEt/DNA-dependent apoptosis and cellular-proliferation inhibition. Consistent with the ASO1-cEt/DNA treatment in Huh7 and HepG2 parent cells (Fig. 3B – Fig. 3E, Supplementary Fig. 2C – Supplementary Fig. 2F), HCC cells expressing luciferase-strawberry also had a significantly higher percentage of Annexin-V-positive cells and a significantly lower percentage of EdU-positive cells upon ASO1-cEt/DNA treatment (Fig. 4B – Fig. 4C, Supplementary Fig. 4B – Supplementary Fig. 4C). Interestingly, expression of T7-PKM2 completely abrogated the ASO1-cEt/DNA-dependent apoptosis effect, but did not affect the ASO1-cEt/DNA-dependent inhibition of cellular proliferation (Fig. 4B – Fig. 4C, Supplementary Fig. 4B – Supplementary Fig. 4C). Confirming

and extending previous studies (24–27), this result indicates that PKM2 confers resistance to apoptosis, whereas PKM1 inhibits cellular proliferation.

Enforced expression of PKM1 is sufficient to reduce HCC cell growth

Given that PKM1 plays a role in cellular-proliferation inhibition, we tested whether enforced expression of PKM1 is sufficient to reduce HCC cell growth. We used a lentiviral expression vector to stably express T7-PKM1 cDNA in both Huh7 and HepG2 cells (Supplementary Fig. 3A – Supplementary Fig. 3C). T7-PKM1 was enzymatically active (Supplementary Fig. 3C). To understand how PKM1 enforced expression affects HCC cell growth, we measured clonogenic growth in soft agar of cells expressing T7-PKM1 or luciferase-strawberry. T7-PKM1-expressing cells formed ~6-fold fewer colonies than luciferase-strawberry-expressing cells, in both Huh7 and HepG2 backgrounds (Supplementary Fig. 4D – Supplementary Fig. 4G). This result demonstrates that enforced expression of PKM1 is sufficient to inhibit HCC cell growth.

ASO1-cEt/DNA alters glucose metabolism in HCC cells

In cells, PKM1 is a constitutively active tetramer, whereas PKM2 is allosterically regulated and exists as a catalytically active tetramer or an inactive dimer or monomer (13,14). In cancer cells, PKM2 is predominantly found as an inactive dimer (36). Considering that ASO1-cEt/DNA switches *PKM* splicing from PKM2 to PKM1 (Fig. 1, Fig. 2, Supplementary Fig. 1), we hypothesized that pyruvate kinase activity in HCC cells would increase upon ASO1-cEt/DNA treatment. To test this hypothesis, we assayed pyruvate kinase activity in HCC cells, with or without ASO treatment. ASO1-cEt/DNA, but not Ctrl-cEt/DNA treatment increased pyruvate kinase activity by ~2-fold and ~4-fold in Huh7 and HepG2 cells, respectively (Fig. 5A, Supplementary Fig. 5A). Given that pyruvate kinase is involved in a rate-limiting step of glycolysis (6,7), the increase in pyruvate kinase activity caused by ASO1-cEt/DNA ought to have an impact on glucose metabolism. To assess the utilization of glucose in glycolysis and the TCA cycle, we conducted stable isotope tracing by incubating cells with uniformly labeled glucose ([U-^{13}C]-glucose), followed by liquid chromatography-mass spectrometry (LC-MS). *De novo* serine (M+3) and glycine (M+2) synthesis from glucose decreased significantly, relative to both the Ctrl-cEt/DNA and NTC controls (Fig. 5B), implying a lower availability of these substrates for one-carbon metabolism and nucleotide synthesis, which are required for cell proliferation and homeostasis. The glycolysis end-product, pyruvate (M+3), can be reduced to lactate (M+3), converted to alanine (M+3), or converted to acetyl-coA before entering the TCA cycle. Upon

ASO1-cEt/DNA treatment, we observed significantly lower incorporation of glucose carbons in lactate (M+3) and alanine (M+3) (Fig. 5B). Furthermore, a significantly higher proportion of glucose carbons was funneled into the TCA cycle, as shown by the increase in the (M+2) isotopologues of TCA-cycle intermediates (Fig. 5B). Taken together, these data show that ASO1-cEt/DNA treatment diverts glucose from anabolic processes necessary for cell proliferation towards oxidative metabolism. In line with the decrease in aerobic glycolysis, we observed a decrease in lactate (M+3) levels in the spent medium upon ASO1-cEt/DNA treatment in Huh7 cells (Supplementary Fig. 5B).

ASO1-cEt/DNA delays liver-tumor growth in a xenograft mouse model

As ASO1-cEt/DNA inhibits cell growth in cultured HCC cells (Fig. 3, Supplementary Fig. 2B – Supplementary Fig. 2F), we explored its *in vivo* efficacy in a xenograft model. We generated the xenograft mouse model by transplanting 2×10^6 luciferase-integrated HepG2 cells into the upper left lobe of the liver in adult NSG mice on Day 0 (Fig. 6A). The tumor was allowed to grow for 10 days prior to the first ASO treatment (Fig. 6A). Tumor growth was tracked using *in vivo* bioluminescence imaging. Luciferase signal was first detected three days after cell transplantation (Fig. 6B, Fig. 6C). Moreover, the luciferase signal increased by day 10, indicating that tumors were actively growing in the liver prior to ASO treatment (Fig. 6C). Significantly lower luciferase signal was detected in ASO1-cEt/DNA-treated mice than in Ctrl-cEt/DNA-treated or saline-treated mice from day 21 to day 29 (Fig. 6B, Fig. 6C). Furthermore, tumors isolated from the liver on day 29 were significantly smaller in ASO1-cEt/DNA-treated mice compared to the control groups (Fig. 6D, Fig. 6E). We also performed immunohistochemistry (IHC) using anti-Ki67 antibody to measure cellular proliferation in the liver tumors, and found that the ASO1-cEt/DNA-treated mice had significantly fewer Ki67-positive cells (Fig. 6F, Fig. 6G). We conclude that ASO1-cEt/DNA inhibits liver-tumor growth in a xenograft mouse model.

Next, we tested whether the tumor-growth inhibition is caused by ASO1-cEt/DNA-induced *PKM* splice-switching in the tumors. First, we assessed by IHC whether the ASO1-cEt/DNA can be effectively delivered to HCC tumors *in vivo*; we detected the ASO with antibody that recognizes the phosphorothioate backbone (52). Although the majority of ASO1-cEt/DNA was taken up by adjacent normal liver, the ASO was also clearly present within the liver tumor, particularly in cells adjacent to blood vessels (Fig. 6H); some ASO was also detectable in Kupffer cells around blood vessels (green arrows; Fig. 6H) and in the nucleus of hepatocytes inside the tumor (red arrows; Fig. 6H).

Using radioactive RT-PCR, we observed an ~18-fold increase in the PKM1 isoform mRNA in liver tumors after ASO1-cEt/DNA treatment, which corresponds to ~2% PKM1 isoform mRNA in total (Fig. 6I). We also analyzed the PKM protein level in the tumor, but we could not consistently observe an increased level of PKM1 protein after ASO1-cEt/DNA treatment (Fig. 6J). This observation could be due to the cells with high PKM1 isoform levels being selected against.

To rule out the possibility that the ASO1-cEt/DNA-dependent liver-tumor growth inhibition is an off-target effect, we tested another ASO, ASO2-cEt/DNA, with a different *PKM* target sequence (Supplementary Fig. 6A). We first tested whether ASO2-cEt/DNA causes *PKM* splice-switching. We transfected HepG2 cells with ASO2-cEt/DNA and analyzed *PKM* alternative splicing by radioactive RT-PCR. ASO2-cEt/DNA induced *PKM* splice-switching, but to a lesser extent than ASO1-cEt/DNA (Supplementary Fig. 6B, Supplementary Fig. 6C). We then tested whether ASO2-cEt/DNA could similarly delay liver-tumor growth in the xenograft mouse model. Indeed, ASO2-cEt/DNA-treated mice had significantly lower luciferase signal from day 21 to day 29, smaller tumors on day 29, and fewer Ki67-positive cells than Ctrl-cEt/DNA-treated or saline-treated mice (Supplementary Fig. 6D - Supplementary Fig. 6I). This result demonstrates that ASO2-cEt/DNA can also delay liver-tumor formation, but is less potent than ASO1-cEt/DNA. Importantly, this experiment confirms that the delayed tumor growth is an on-target response.

Considering that enforced expression of PKM1 was sufficient to slow down HCC cell growth *in vitro* (Supplementary Fig. 4D – Supplementary Fig. 4G), we wished to test whether it can affect liver-tumor growth *in vivo*. To this end, we transplanted HepG2 cells stably expressing T7-PKM1 into the upper left lobe of the liver in adult NSG mice. Significantly smaller liver tumors developed in mice injected with T7-PKM1-expressing cells, compared to luciferase-strawberry-expressing cells (Supplementary Fig. 6J, Supplementary Fig. 6K), showing that ectopic expression of PKM1 is sufficient to delay liver-tumor formation *in vivo*.

***Pkm*-targeted ASO therapy can also inhibit HCC growth in a genetic mouse model**

Considering the limitations of xenograft models, we analyzed whether *Pkm*-targeted ASO treatment can be applied to treat HCC in genetically engineered mice. To establish the mouse model, we used the Sleeping Beauty transposon system (37) to transpose a human c-Myc proto-oncogene cDNA into the genome of hepatocytes in mice. Briefly, we performed hydrodynamic tail-vein injection to deliver the Sleeping Beauty transposase and c-Myc plasmids to hepatocytes in FVB/N mice on day 0 (Fig. 7A). This allows the hepatocytes to amplify c-Myc, which is found in 40%-60% of early HCC human samples (38), and induces liver tumor formation in FVB/N

mice (37). Liver tumors were allowed to form before the first mASO treatment on day 28 (Fig. 7A). The mASO (mASO3-cEt/DNA) used for this experiment was identified as the most potent mASO to induce *mPkm* splice-switching after systematic screening of ASOs in cell culture (data not shown). As an example of its activity *in vitro*, mASO3-cEt/DNA transfected into HepA1-6 cells stimulated *mPkm* splice-switching from mPKM2 to mPKM1, at both mRNA and protein levels (Supplementary Fig. 7A – Supplementary Fig. 7C). For the *in vivo* experiments, after three weeks of mASO treatment, we euthanized the mice on day 47 and measured the weight of the tumors relative to their liver (weight of tumor/liver). We found that mASO3-cEt/DNA-treated mice had a significantly smaller tumor/liver weight ratio, compared to saline-treated or Ctrl-cEt/DNA-treated mice (Fig. 7B, Fig. 7C). In addition, we detected a significant increase in *mPKM1* mRNA level upon mASO-cEt/DNA treatment (Fig. 7D, Fig. 7E).

Surprisingly, we noticed that female mice (Fig. 7B, red dots) had a more potent response to mASO3-cEt/DNA treatment than male mice (Fig. 7B, blue dots). Consistent with human liver-cancer data showing that men are more susceptible to liver cancer than women (4), female mice had less aggressive and smaller liver tumors than male mice, as seen in the saline-treated and Ctrl-cEt/DNA-treated groups (Fig. 7B). This different susceptibility could account for the difference in the response to mASO3-cEt/DNA treatment between male and female mice.

Previous studies demonstrated that targeted delivery of ASOs to hepatocytes in the liver can significantly enhance their potency (39,40). Liver-targeting ASOs are typically conjugated with triantennary *N*-acetylgalactosamine (GN3), which facilitates receptor-mediated endocytosis upon binding to asialoglycoprotein receptor (ASGP-R), a receptor that is exclusively expressed in hepatocytes (41). Thus, we tested whether GN3-conjugation to mASO3-cEt/DNA (mASO3-GN3-cEt/DNA) can improve the ASO potency in HCC tumor-growth inhibition in the genetic mouse model. Surprisingly, mASO3-GN3-cEt/DNA was slightly less potent than the unconjugated mASO3-cEt/DNA (Supplementary Fig. 7D, Supplementary Fig. 7E). Because the expression of ASGP-R is down-regulated in highly dedifferentiated human HCC tumor tissue (42), we analyzed the protein level of ASGP-R in HCC tumors obtained from the genetic mouse model. ASGPR1, a functional subunit of ASGP-R, was not detectable by western blot in HCC tumors (Supplementary Fig. 7F). This result explains why GN3-conjugation could not improve the potency of mASO3-cEt/DNA in mice.

Given that mASO3-cEt/DNA inhibited HCC tumor growth (Fig. 7B, Fig. 7C), we analyzed whether it improved the survival of HCC-tumor-bearing mice. Tumor-bearing mice (n=42), with equal gender ratio, were randomly assigned to receive saline, Ctrl-cEt/DNA, or mASO3-cEt/DNA, following the dosing schedule (Fig. 7A). Mice were euthanized if tumors grew larger

than 20 mm. We found that mASO-cEt/DNA-treated mice had significantly longer median survival (61.5 days; p-value 0.0001) compared to saline-treated mice (45.0 days) or Ctrl-cEt/DNA-treated mice (45.5 days) (Fig. 7F). This result further confirms that mASO3-cEt/DNA delays HCC tumor growth.

Lastly, we checked whether mASO3-cEt/DNA causes any toxicity in non-tumor-bearing mice. We treated wild-type FVB/N mice with either mASO3-cEt/DNA or saline for three weeks, followed by IHC analysis in different organs. During the three weeks of treatment, no obvious gross abnormalities were observed. Furthermore, we did not detect any histological abnormalities in the various organs in either mASO-cEt/DNA-treated or saline-treated mice after three weeks of treatment (Fig. 7G). This observation suggests that mASO3-cEt/DNA is well tolerated in wild-type FVB/N mice. Taken together, these promising results demonstrate that mASO-cEt/DNA effectively inhibits HCC tumor growth in mice, without obvious toxicity.

Discussion

Liver cancer is an aggressive and lethal disease. There are more than 800,000 liver-cancer deaths per year, which is close to its annual incidence worldwide (1,2,4). The major risk factors of liver cancer are alcohol consumption, obesity, diabetes, tobacco smoking, hepatitis B virus (HBV) infection, and hepatitis C virus (HCV) infection (4). Given the absence of signs and symptoms in the early stages of liver cancer, most patients are not diagnosed until the later stages, when curative treatments are no longer possible. There are currently several systemic therapies for advanced-stage HCC, including two multiple-kinase inhibitors, Sorafenib and Lenvatinib, as first-line treatment options (4,5). Moreover, the U.S. Food and Drug Administration approved a monoclonal antibody (Ramucirumab), an immune-checkpoint inhibitor (Nivolumab), a multi-kinase inhibitor (Regorafenib), and a tyrosine-kinase inhibitor (Carbozantinib) as second-line treatments for HCC patients who are refractory to Sorafenib (4,5). However, none of these systemic therapies drastically improves patient outcomes. Thus, new breakthrough treatments are sorely needed. In this study, we demonstrated that ASO-based *PKM* splice-switching therapy inhibits HCC tumor growth in different pre-clinical models, including cell culture, and xenograft and genetic mouse models (Fig. 3, Fig. 6, Fig. 7, Supplementary Fig. 2). These results highlight the potential of ASO-based *PKM* splice-switching therapy as a novel treatment to address the major unmet needs in HCC management.

Down-regulation of *PKM2* induces apoptosis of cancer cells, both *in vivo* and *in vitro* (24–26), suggesting that PKM2 could be a therapeutic target. Moreover, we demonstrated that enforcing expression of PKM1 is sufficient to reduce HCC cell growth (Supplementary Fig. 4),

which is consistent with the tumor suppressor activity previously observed for PKM1 (27). Intriguingly, several studies reported that PKM2 is not required to promote tumorigenesis, and loss of PKM2 might even promote tumor progression (43,44); however, most cells that promoted tumor formation were PKM1-negative (43,44), suggesting that PKM2 depletion alone might not be sufficient to obtain a significant anti-tumor effect. It was further reported that PKM2 might play a role in maintaining metabolic homeostasis to prevent liver inflammation that eventually leads to HCC (44). Unlike PKM2 siRNA or shRNA knockdown approaches, or gene therapy to force PKM1 expression, our ASO-based PKM splice-switching strategy can simultaneously decrease PKM2 and increase PKM1, which promotes apoptosis and magnifies the anti-tumor effect stemming from PKM1's tumor suppressor activity. This dual effect is achieved by delivering a single therapeutic agent. Furthermore, ASO-based therapy has the flexibility to be withdrawn or the dosage reduced if toxicity is observed during treatment.

Previous studies revealed that PKM2 is overexpressed in liver tumors (TCGA database; (11,32). In addition, we observed that PKM2 is overexpressed in HCC cell lines, relative to normal adult liver (Supplementary Fig. 1). Thus, *PKM* pre-mRNA is upregulated during liver tumorigenesis and this expression pattern allows the ASO to target *PKM* pre-mRNA in liver tumors versus in normal hepatocytes, reducing potential on-target liver toxicity. Indeed, there was no apparent toxicity in mice upon ASO treatment, even though the ASO accumulates in normal adjacent liver (Fig. 6H, Fig. 7G). The efficacy of ASO-based *PKM* splice-switching therapy would presumably increase if a method becomes available to specifically target ASOs to HCC tumors. Regarding off-target liver toxicity, we previously demonstrated that the choice of ASO chemistry and delivery method can significantly influence the extent of off-target activity (45). In that study, ASO1 with cEt/DNA mixed-chemistry had greater specificity than uniformly modified MOE ASOs (45). Furthermore, delivering ASOs by free uptake in cell lines, or subcutaneously in mice, substantially reduced off-target activity (45).

In contrast to current HCC therapeutic approaches that target blood-vessel development, the immune system, or cell signaling, the ASO-based *PKM* splice-switching therapy described here increases pyruvate-kinase activity in HCC cells and alters their glucose metabolism (Fig. 5, Supplementary Fig. 5). This is a distinct strategy to inhibit HCC tumor growth. It will be interesting to test whether combining the ASO-based *PKM* splice-switching therapy with any of the current advanced-stage HCC therapies improves patient outcomes and shows clinical benefits. Alternatively, the ASO-based *PKM* splice-switching therapy could be combined with chemotherapy to treat patients with intermediate-stage HCC. It has been suggested that PKM2 confers chemotherapy resistance to cancer cells (46). Moreover, down-regulation of PKM2

reduces chemoresistance of advanced bladder cancer to cisplatin, and of HCC cells to doxorubicin (47,48). These observations indicate the potential of ASO-based *PKM* splice-switching therapy as a combination therapy, in addition to stand-alone therapy.

Consistent with a previous study showing that enhancement of PKM2 activity by a class of small-molecule activators reduces glucose-carbon flow into the serine-biosynthetic pathway (49), we observed that increasing pyruvate kinase activity by ASO-based *PKM* splice-switching diverts glucose carbon from the serine-biosynthesis pathway to the TCA cycle (Fig. 5). This metabolic switch decreases the availability of the substrates for nucleotide synthesis required for cell proliferation. Considering that our ASOs only partially switch PKM2 to PKM1, a combined ASO and small-molecule activator treatment may be more effective than either treatment alone.

Interestingly, depleting PKM2 by Cre-Lox excision of exon 10 in mouse embryonic fibroblasts (MEFs) resulted in compensatory expression of PKM1, which inhibited cellular proliferation by altering nucleotide synthesis (27). Furthermore, supplementing the growth medium with thymine rescued the cell-proliferation inhibition (27). In the future, it will be interesting to examine whether supplementation with exogenous nucleotides or amino acids can rescue the ASO-dependent HCC tumor slow-growth phenotype, both *in vivo* and *in vitro*. This might shed light on the mechanisms through which ASO-based *PKM* splice-switching inhibits HCC tumor growth.

There is mounting evidence that post-translationally modified PKM2 can translocate into the nucleus to function as a transcriptional co-activator that regulates transcription with several transcription factors, including hypoxia-inducible factor-1α (HIF-1α), octamer-binding transcription factor 4 (OCT4), signal transducer and activator of transcription 3 (STAT3), and β-catenin (18). Furthermore, nuclear PKM2 has been implicated in genomic instability, maintenance of cancer stemness, cancer metastasis, and tumor angiogenesis (18). Considering that ASO-based *PKM* splice-switching treatment tends to decrease the PKM2 isoform (Fig. 1, Fig. 2, Supplementary Fig. 1), it will be interesting to investigate how the ASO treatment might affect each of PKM2's non-canonical nuclear functions. Given our promising results with multiple pre-clinical HCC models, the next logical steps will be to evaluate the safety and efficacy of the lead ASO in non-human primates, in preparation for eventual clinical trials.

Material and Methods

Antisense Oligonucleotides

All ASOs used in this study are listed in Table S1. Mixed-chemistry oligonucleotides consist of a mixture of constrained-ethyl (cEt) and DNA nucleotides, as shown in Table S1, and were synthesized as described (34). GalNAc-conjugated ASOs were synthesized, purified, and quantified as described (39). All ASOs had uniform phosphorothioate backbones and 5-methyl C. We dissolved the ASOs in water and stored them at −20 °C. Oligonucleotide concentration was determined with a Nanodrop spectrophotometer.

Cell Culture and ASO Delivery

HepG2 hepatocellular carcinoma cells were cultured in EMEM (ATCC) supplemented with 10% FBS and 1% Penicillin/Streptomycin (P/S) at 37 °C/5% CO_2. Huh7 hepatocellular carcinoma cells were maintained in RPMI 1640 (Corning) supplemented with 20% FBS and 1% P/S. HepA1-6 mouse hepatocellular carcinoma cells were cultured in DMEM (Corning) supplemented with 10% FBS and 1% P/S. ASOs were delivered to HepG2 and Huh7 cells using Lipofectamine 2000 (Invitrogen) at a final concentration of 60 nM. Alternatively, ASOs were added directly to the culture medium without any delivery reagent (free uptake), at the indicated concentrations for 4 to 7 days.

Plasmids and Stable Cell Lines

cDNA was prepared from RNA extracted from U87 glioblastoma cells after treating with or without 60 nM ASO1-cEt/DNA in the presence of lipofectamine transfection reagent for two days (30). PKM2 cDNA sequence was amplified from U87-cell RNA without any ASO treatment. PKM1 and PKMds cDNA sequences were amplified from U87-cell RNA after ASO treatment. The amplified cDNA for each isoform was cloned into a lentiviral backbone (PGK-EF1α vector, kindly provided by Scott Lyons, CSHL), which contains a puromycin selection marker, by conventional cloning into the Pacl restriction site. Lentiviruses were produced in HEK293T/17 cells by co-transfecting viral constructs with psPAX2 and vesicular stomatitis virus G glycoprotein (VSVG). Viral supernatant was collected 48–72 h post-transfection, filtered, and stored at -80 °C. HepG2 and Huh7 cells were infected with lentiviral particles overnight, in the presence of 8 μg/ml polybrene (Sigma) and selected using 1.5 – 3 μg/ml puromycin (Sigma) for at least two weeks to generate stable cell lines.

Animals and Tumor Models

Non-obese diabetic-severe combined immunodeficiency (NOD-SCID)-gamma (NSG) immunocompromised mice (strain 005557; The Jackson Laboratory) were housed in vented cages and bred in-house. HepG2 orthotopic xenograft tumors were established as described (50). A subcostal transversal abdominal incision was performed, and 2×10^6 luciferase-integrated HepG2 cells (40,000 cells/μl in Hank's balanced salt solution) were injected into the upper left lobe of the liver in adult NSG mice. Tumor growth was tracked using *in vivo* bioluminescence imaging. The implanted mice were given luciferase substrate, 200 mg/kg D-luciferin (GOLDBIO), by intraperitoneal injection 12 min prior to imaging. Tumors were allowed to grow, as verified by the increasing luciferase signal, for 10 days prior to the first ASO treatment. ASOs were delivered by subcutaneous (s.c.) injection at 250 mg/kg/wk with five consecutive-day injections, followed by two-days rest, for three weeks. All animal protocols were performed in accordance with Cold Spring Harbor Laboratory's Institutional Animal Care and Use Committee (IACUC) guidelines.

Hydrodynamic Tail Vein Injection

A mixture of 5 μg pT3-EF1a-Myc and 1 μg pCMV-SB13 Transposase (a kind gift from Dr. Xin Chen, University of California at San Francisco; (37)) in sterile 0.9% NaCl solution was prepared. The plasmid mixture was injected into the lateral tail vein of FVB/N mice, with a total volume corresponding to 10% of body weight in 5-7 seconds.

Radioactive RT-PCR and RT-qPCR

Total RNA was extracted from cells or tissue using TRIzol (Invitrogen) and reverse-transcribed with ImProm-II reverse transcriptase (Promega) using oligo-dT primers. *PKM* cDNA was amplified with AmpliTaq DNA polymerase (Thermo Fisher) using Fwd 5'-AGAAACAGCCAAAGGGGACT-3' primer that sits on exon 8 and Rev 5'-CATTCATGGCAAAGTTCACC -3' primer that sits on exon 11, in the presence of radiolabeled [α-^{32}P]-dCTP. For *mPKM* cDNA, Fwd: 5'-AAACAGCCAAGGGGGACTAC-3' and Rev: 5'-CGAGCAGTCTGGGGATTTCG-3' were used. The radiolabeled PCR product was digested with PstI (NEB) for 2 hrs at 37 °C to distinguish *PKM1* (undigested) from *PKM2* (cleaved into 2 bands) (30). Samples were then separated on a 5% native polyacrylamide gel (Bio-Rad), visualized by autoradiography on a Typhoon 9410 phosphoimager (GE Healthcare), and quantified using ImageJ. The radioactive signal of each band was normalized to the G/C content to calculate relative changes in splice isoforms. For RT-qPCR, the cDNA was analyzed on a QuantStudio 6 Flex Real-Time PCR system (ThermoFisher Scientific). Fold changes were calculated using the ΔΔCq method (51). Primer sequences included PKM1 Fwd: 5'-

CCCACTCGGGCTGAAGGCAGTG-3', PKM1 Rev: 5'-GCTGCCTCAGCCTCACGAGC-3', PKM2 Fwd: 5'-CCCACTCGGGCTGAAGGCAGTG-3', PKM2 Rev: 5'-GGCAGCCTCTGCCTCACGGG-3', PKM total Fwd: 5'-CCCACTCGGGCTGAAGGCAGTG-3', PKM total Rev: 5'-GGTGCTGCATGCGCACAGCC-3', PKLR Fwd: 5'-CGGGTGCAATTTGGCATTGA-3', PKLR Rev: 5'-AAGGGATGGGGTACAAGGGT-3', HPRT Fwd: 5'-TGACCAGTCAACAGGGGACA-3' and HPRT Rev: 5'-TGCCTGACCAAGGAAAGCAA-3'

Western Blotting

Cells and tissues were harvested and processed as described (52). Protein lysates were separated on SDS-PAGE and transferred onto nitrocellulose membranes. The membrane was blocked with 5% milk in TBST and incubated overnight at 4 °C with primary antibody rb-PKM1 (1:300; Proteintech), rb-PKM2 (1:500; Cell Signaling), rb-PKM total (1:500; Cell Signaling), rb-ASGP-R1 (1:6,000; ProteinTech), ms-T7 (1:250; CSHL), or ms-α-tubulin (1:10,000; Sigma). The membrane was then incubated with goat-anti-mouse and goat anti-rabbit Li-Cor IRDye 800 (green) and 680 (red) secondary antibodies (1:10,000; Li-Cor) for 1 h at room temperature. Protein bands were visualized on an Odyssey imaging system (Li-Cor) and quantified using ImageStudio and ImageJ.

EdU and Annexin V Staining Assays

Cells (3.75×10^3 cells/well) were seeded onto eight-well culture slides (Falcon) and treated with 20 μM ASO via free uptake for four days. To measure Annexin V positive cells, Alexa Fluor 488 Annexin V/Dead Cell Apoptosis Kit (Invitrogen) was used in accordance with the manufacturer's instructions. For EdU staining, 10 μM EdU was added to the cells on day 5 and incubated at 37 °C for two hours. EdU incorporation was measured using a Click-it Plus EdU Alexa Fluor 594 Imaging Kit (Invitrogen) in accordance with the manufacturer's instructions. Images were captured on a Zeiss Observer microscope. All images within the same figure panel were taken with the same exposure setting and identically processed using ImageJ and Adobe Photoshop.

Soft Agar Assay

HepG2 (10×10^3 cells/well) or Huh7 (50×10^3 cells/well) cell suspension was incubated in an upper layer of 0.3% agarose (ThermoFisher Scientific) in EMEM with 10% FBS and 1% P/S or RPMI 1640 with 20% FBS and 1% P/S, respectively. The HepG2 or Huh7 suspension with agarose was overlaid on 0.6% solidified basal agar with EMEM with 10% FBS and 1% P/S or RPMI 1640

with 20% FBS and 1% P/S, respectively, in a six-well plate. The plate was placed at room temperature until the top agarose solidified. The plate was then incubated at 37 °C/5% CO_2 for at least 3 weeks, before staining with crystal violet. Visible colonies were then counted.

IHC

Harvested tissues were treated as described (52). Primary rb-ASO (1:10,000; Ionis Pharmaceuticals) or rb-Ki67 (1:200; Spring Bioscience) antibody was incubated with the slides at room temperature for 1 h. The signal was visualized with HRP-labeled anti-rabbit polymer (DAKO) and DAB (DAKO). Slides were counterstained with hematoxylin (Sigma).

Pyruvate Kinase Assay

Pyruvate kinase activity was measured with a Pyruvate Kinase Activity Colorimetric/Fluorometric Assay Kit (BioVision) in accordance with the manufacturer's instructions. Cells were treated with 20 μM ASO by free uptake for four days and lysed in assay buffer. The lysate was incubated with or without 5 mM FBP for 30 min at room temperature prior to analysis. Optical density at 570 nm was measured at room temperature using a SpectraMax i3 plate reader (Molecular Devices) from 0 min – 20 min with 1-min interval time points.

Stable Isotope Tracing by LC-MS

Cells (5×10^4 cells/well) were seeded in 6-well plates and treated with 20 μM ASO by free uptake for seven days. Medium was replaced and ASO replenished on day 4. On day 7, the cell-culture medium was replaced with glucose-free medium containing uniformly labeled [U-^{13}C]-glucose (2000 mg/L) 8 h prior to collecting intracellular metabolites. Extracts and media from five independent cell cultures were analyzed for each condition. Briefly, after quick removal of the culture medium, cells were washed in PBS before adding extraction solution (50% methanol, 30% acetonitrile, 20% H_2O) and then scraped. After centrifugation to remove the precipitated proteins and insoluble debris, the supernatants were collected and stored in autosampler vials at -80°C until analysis. Samples were randomized to avoid bias due to machine drift, and processed blindly. LC-MS analysis was performed using a Vanquish Horizon UHPLC system coupled to a Q Exactive HF mass spectrometer (both Thermo Fisher Scientific). Sample extracts were analyzed as previously described (53). The acquired spectra were analyzed using XCalibur Qual Browser and XCalibur Quan Browser software (Thermo Fisher Scientific) by referencing to an internal library of compounds. Metabolite peak areas were corrected for natural ^{13}C abundance using the R package AccuCor (54). To calculate isotopologue distribution, corrected peak areas

of each metabolite's isotopologues were normalized to the total metabolite pool (sum of all isotopologues of a given metabolite). Values of release of lactate were adjusted to cell density upon background subtraction.

References

1. Torre LA, Bray F, Siegel RL, Ferlay J, Lortet-Tieulent J, Jemal A. Global cancer statistics, 2012. CA Cancer J Clin. 2015;65:87–108.
2. Jemal A, Ward EM, Johnson CJ, Cronin KA, Ma J, Ryerson B, et al. Annual Report to the Nation on the Status of Cancer, 1975-2014, Featuring Survival. J Natl Cancer Inst. 2017;109.
3. Llovet JM, Zucman-Rossi J, Pikarsky E, Sangro B, Schwartz M, Sherman M, et al. Hepatocellular carcinoma. Nat Rev Dis Prim. 2016;2:16018.
4. Villanueva A. Hepatocellular Carcinoma. N Engl J Med. 2019;380:1450–62.
5. Llovet JM, Montal R, Sia D, Finn RS. Molecular therapies and precision medicine for hepatocellular carcinoma. Nat Rev Clin Oncol. 2018;15:599–616.
6. Vander Heiden MG, Cantley LC, Thompson CB. Understanding the warburg effect: The metabolic requirements of cell proliferation. Science (80-.). 2009. page 1029–33.
7. Koppenol WH, Bounds PL, Dang C V. Otto Warburg's contributions to current concepts of cancer metabolism. Nat. Rev. Cancer. 2011. page 325–37.
8. Noguchi T, Yamada K, Inoue H, Matsuda T, Tanaka T. The L- and R-type isozymes of rat pyruvate kinase are produced from a single gene by use of different promoters. J Biol Chem. 1987;262:14366–71.
9. Noguchi T, Inoue H, Tanaka T. The M1- and M2-type isozymes of rat pyruvate kinase are produced from the same gene by alternative RNA splicing. J Biol Chem. 1986;261:13807–12.
10. Clower C V., Chatterjee D, Wang Z, Cantley LC, Heidena MG Vander, Krainer AR. The alternative splicing repressors hnRNP A1/A2 and PTB influence pyruvate kinase isoform expression and cell metabolism. Proc Natl Acad Sci U S A. 2010;107:1894–9.
11. Bluemlein K, Grüning N-M, Feichtinger RG, Lehrach H, Kofler B, Ralser M. No evidence for a shift in pyruvate kinase PKM1 to PKM2 expression during tumorigenesis. Oncotarget. 2011;2:393–400.
12. Christofk HR, Vander Heiden MG, Harris MH, Ramanathan A, Gerszten RE, Wei R, et al. The M2 splice isoform of pyruvate kinase is important for cancer metabolism and tumour growth. Nature. 2008;452:230–3.
13. Dombrauckas JD, Santarsiero BD, Mesecar AD. Structural basis for tumor pyruvate kinase M2 allosteric regulation and catalysis. Biochemistry. 2005;44:9417–29.
14. Harris RA, Fenton AW. A critical review of the role of M2PYK in the Warburg effect. Biochim Biophys acta Rev cancer. 2019;1871:225–39.
15. Christofk HR, Vander Heiden MG, Wu N, Asara JM, Cantley LC. Pyruvate kinase M2 is a phosphotyrosine-binding protein. Nature. 2008;452:181–6.
16. Anastasiou D, Poulogiannis G, Asara JM, Boxer MB, Jiang J, Shen M, et al. Inhibition of pyruvate kinase M2 by reactive oxygen species contributes to cellular antioxidant responses. Science. 2011;334:1278–83.
17. Hitosugi T, Kang S, Vander Heiden MG, Chung T-W, Elf S, Lythgoe K, et al. Tyrosine phosphorylation inhibits PKM2 to promote the Warburg effect and tumor growth. Sci Signal. 2009;2:ra73.
18. Amin S, Yang P, Li Z. Pyruvate kinase M2: A multifarious enzyme in non-canonical localization to promote cancer progression. Biochim. Biophys. Acta - Rev. Cancer. Elsevier B.V.; 2019. page 331–41.
19. Boxer MB, Jiang J, Vander Heiden MG, Shen M, Skoumbourdis AP, Southall N, et al. Evaluation of substituted N,N'-diarylsulfonamides as activators of the tumor cell specific M2 isoform of pyruvate kinase. J Med Chem. 2010;53:1048–55.
20. Jiang J, Boxer MB, Vander Heiden MG, Shen M, Skoumbourdis AP, Southall N, et al. Evaluation of thieno[3,2-b]pyrrole[3,2-d]pyridazinones as activators of the tumor cell specific M2 isoform of pyruvate kinase. Bioorg Med Chem Lett. 2010;20:3387–93.

21. Adem S, Comakli V, Uzun N. Pyruvate kinase activators as a therapy target: a patent review 2011-2017. Expert Opin. Ther. Pat. Taylor and Francis Ltd; 2018. page 61–8.
22. Anastasiou D, Yu Y, Israelsen WJ, Jiang JK, Boxer MB, Hong BS, et al. Pyruvate kinase M2 activators promote tetramer formation and suppress tumorigenesis. Nat Chem Biol. 2012;8:839–47.
23. Yoon YJ, Kim YH, Jin Y, Chi SW, Moon JH, Han DC, et al. 2′-hydroxycinnamaldehyde inhibits cancer cell proliferation and tumor growth by targeting the pyruvate kinase M2. Cancer Lett. Elsevier Ireland Ltd; 2018;434:42–55.
24. Goldberg MS, Sharp PA. Pyruvate kinase M2-specific siRNA induces apoptosis and tumor regression. J Exp Med. 2012;209:217–24.
25. Morfouace M, Lalier L, Oliver L, Cheray M, Pecqueur C, Cartron PF, et al. Control of glioma cell death and differentiation by PKM2-Oct4 interaction. Cell Death Dis. Nature Publishing Group; 2014;5.
26. Liang J, Cao R, Wang X, Zhang Y, Wang P, Gao H, et al. Mitochondrial PKM2 regulates oxidative stress-induced apoptosis by stabilizing Bcl2. Cell Res. 2017;27:329–51.
27. Lunt SY, Muralidhar V, Hosios AM, Israelsen WJ, Gui DY, Newhouse L, et al. Pyruvate kinase isoform expression alters nucleotide synthesis to impact cell proliferation. Mol Cell. 2015;57:95–107.
28. Nomakuchi TT, Rigo F, Aznarez I, Krainer AR. Antisense oligonucleotide-directed inhibition of nonsense-mediated mRNA decay. Nat Biotechnol. Nature Publishing Group; 2016;34:164–6.
29. Bennett CF, Swayze EE. RNA targeting therapeutics: molecular mechanisms of antisense oligonucleotides as a therapeutic platform. Annu Rev Pharmacol Toxicol. 2010;50:259–93.
30. Wang Z, Jeon HY, Rigo F, Bennett CF, Krainer AR. Manipulation of PK-M mutually exclusive alternative splicing by antisense oligonucleotides. Open Biol. 2012;2:120133.
31. Geary RS, Norris D, Yu R, Bennett CF. Pharmacokinetics, biodistribution and cell uptake of antisense oligonucleotides. Adv Drug Deliv Rev. 2015;87:46–51.
32. Wong CCL, Au SLK, Tse APW, Xu IMJ, Lai RKH, Chiu DKC, et al. Switching of pyruvate kinase isoform l to M2 promotes metabolic reprogramming in hepatocarcinogenesis. PLoS One. Public Library of Science; 2014;9.
33. Mendez-Lucas A, Li X, Hu J, Che L, Song X, Jia J, et al. Glucose catabolism in liver tumors induced by c-MYC can be sustained by various PKM1/PKM2 ratios and pyruvate kinase activities. Cancer Res. American Association for Cancer Research Inc.; 2017;77:4355–64.
34. Seth PP, Siwkowski A, Allerson CR, Vasquez G, Lee S, Prakash TP, et al. Short antisense oligonucleotides with novel 2′-4′ conformationaly restricted nucleoside analogues show improved potency without increased toxicity in animals. J Med Chem. 2009;52:10–3.
35. Chen M, David CJ, Manley JL. Concentration-dependent control of pyruvate kinase M mutually exclusive splicing by hnRNP proteins. Nat Struct Mol Biol. 2012;19:346–54.
36. Mazurek S, Boschek CB, Hugo F, Eigenbrodt E. Pyruvate kinase type M2 and its role in tumor growth and spreading. Semin Cancer Biol. 2005;15:300–8.
37. Yant SR, Park J, Huang Y, Mikkelsen JG, Kay MA. Mutational analysis of the N-terminal DNA-binding domain of sleeping beauty transposase: critical residues for DNA binding and hyperactivity in mammalian cells. Mol Cell Biol. 2004;24:9239–47.
38. Kaposi-Novak P, Libbrecht L, Woo HG, Lee YH, Sears NC, Conner EA, et al. Central role of c-Myc during malignant conversion in human hepatocarcinogenesis. Cancer Res. 2009;69:2775–82.
39. Prakash TP, Graham MJ, Yu J, Carty R, Low A, Chappell A, et al. Targeted delivery of antisense oligonucleotides to hepatocytes using triantennary N-acetyl galactosamine improves potency 10-fold in mice. Nucleic Acids Res. 2014;42:8796–807.

40. Kim Y, Jo M, Schmidt J, Luo X, Prakash TP, Zhou T, et al. Enhanced Potency of GalNAc-Conjugated Antisense Oligonucleotides in Hepatocellular Cancer Models. Mol Ther. 2019;
41. Stockert RJ. The asialoglycoprotein receptor: relationships between structure, function, and expression. Physiol Rev. 1995;75:591–609.
42. Shi B, Abrams M, Sepp-Lorenzino L. Expression of asialoglycoprotein receptor 1 in human hepatocellular carcinoma. J Histochem Cytochem. 2013;61:901–9.
43. Israelsen WJ, Dayton TL, Davidson SM, Fiske BP, Hosios AM, Bellinger G, et al. XPKM2 isoform-specific deletion reveals a differential requirement for pyruvate kinase in tumor cells. Cell. Cell Press; 2013;155:397.
44. Dayton TL, Gocheva V, Miller KM, Israelsen WJ, Bhutkar A, Clish CB, et al. Germline loss of PKM2 promotes metabolic distress and hepatocellular carcinoma. Genes Dev. Cold Spring Harbor Laboratory Press; 2016;30:1020–33.
45. Scharner J, Ma WK, Zhang Q, Lin K-T, Rigo F, Bennett CF, et al. Hybridization-mediated off-target effects of splice-switching antisense oligonucleotides. Nucleic Acids Res. 2020;48:802–16.
46. Calabretta S, Bielli P, Passacantilli I, Pilozzi E, Fendrich V, Capurso G, et al. Modulation of PKM alternative splicing by PTBP1 promotes gemcitabine resistance in pancreatic cancer cells. Oncogene. 2016;35:2031–9.
47. Wang X, Zhang F, Wu XR. Inhibition of Pyruvate Kinase M2 Markedly Reduces Chemoresistance of Advanced Bladder Cancer to Cisplatin. Sci Rep. Nature Publishing Group; 2017;7.
48. Pan C, Wang X, Shi K, Zheng Y, Li J, Chen Y, et al. MiR-122 reverses the doxorubicin-resistance in hepatocellular carcinoma cells through regulating the tumor metabolism. PLoS One. Public Library of Science; 2016;11.
49. Kung C, Hixon J, Choe S, Marks K, Gross S, Murphy E, et al. Small molecule activation of PKM2 in cancer cells induces serine auxotrophy. Chem Biol. 2012;19:1187–98.
50. Saborowski A, Saborowski M, Davare MA, Druker BJ, Klimstra DS, Lowe SW. Mouse model of intrahepatic cholangiocarcinoma validates FIG-ROS as a potent fusion oncogene and therapeutic target. Proc Natl Acad Sci U S A. 2013;110:19513–8.
51. Rao X, Huang X, Zhou Z, Lin X. An improvement of the 2ˆ(-delta delta CT) method for quantitative real-time polymerase chain reaction data analysis. Biostat Bioinforma Biomath. 2013;3:71–85.
52. Scharner J, Qi S, Rigo F, Bennett CF, Krainer AR. Delivery of GalNAc-Conjugated Splice-Switching ASOs to Non-hepatic Cells through Ectopic Expression of Asialoglycoprotein Receptor. Mol Ther Nucleic Acids. 2019;16:313–25.
53. MacKay GM, Zheng L, Van Den Broek NJF, Gottlieb E. Analysis of Cell Metabolism Using LC-MS and Isotope Tracers. Methods Enzymol. Academic Press Inc.; 2015. page 171–96.
54. Su X, Lu W, Rabinowitz JD. Metabolite Spectral Accuracy on Orbitraps. Anal Chem. 2017;89:5940–8.

Acknowledgements

We thank Shauna Houlihan, Chun-Hao Huang, and Scott Lowe from Memorial Sloan Kettering Cancer Center for providing the plasmids and protocol for hydrodynamic tail vein injection, and Scott Lyon from CSHL for providing the lentiviral vector backbone. We also thank Phyllis Gimotty from the University of Pennsylvania Perlman School of Medicine for advice on statistical analyses and John Erby Wilkinson from University of Michigan for advice on histology analyses. We acknowledge support from NCI Program Project Grant CA13106, and assistance from the CSHL Shared Resources, funded in part by NCI Cancer Center Support Grant 5P30CA045508.

Author Contributions

Conceptualization, W.K.M., J.S., A.R.K.; Investigation, W.K.M., A.S.H.C., H.Y.J., M.J., F.R.; Writing – Original Draft W.K.M.; Writing – Review & Editing, W.K.M., A.R.K., R.M., F.R., C.F.B.; Resources, A.R.K., R.M., F.R., C.F.B.; Supervision, A.R.K.

[FR did original screens for mouse ASOs; Hyun did the human intron 9 ASO screen.

Conflict of Interest Statement

F.R. and C.F.B. are employees of Ionis Pharmaceuticals and own stock options. F.R., C.F.B., and A.R.K. are inventors on patent applications covering the use of PKM ASOs.

Table S1. ASOs used in this study

ASO name	Length	Sequence 5'-3'	Chemistry
ASO1-cEt/DNA	18 nt	AGGCGGCGGAGTTCCTCA	kkddkddkddkddkddkk
ASO2-cEt/DNA	16 nt	GAGGACGATTATGGCC	kkddkddkddkddkddkk
Ctrl-cEt/DNA	18 nt	CGGATGAGTGCCTGCAAT	kkddkddkddkddkddkk
mASO3-cEt/DNA	16 nt	ACTTGGTGAGCACGAT	kddkddkddkddkddk
mASO3-GN3-cEt/DNA	16 nt	ACTTGGTGAGCACGAT	5'GalNAc3-kddkddkddkddkddk

Base modification: k = constrained ethyl (cEt) base modification; d = DNA base; ligand conjugation: GalNAc3 = triantennary *N*-acetylgalactosamine; all ASOs have uniform P=S backbone and 5-methyl-C modifications

Figure legends

Figure 1. Delivery of ASO1-cEt/DNA via lipofectamine induces *PKM* splice switching in Huh7 cells

(A) Radioactive RT-PCR shows the extent of *PKM* splice switching after transfecting Huh7 cells with 60 nM ASO for two days. No-treatment control (NTC) with or without reverse transcriptase (+ RT or – RT, respectively) and a control ASO (Ctrl-cEt/DNA) with four mismatch nucleotides to *PKM* exon 10 were used as controls. (B) Quantification of PKM1 and PKMds isoforms in panel (A). (C) RT-qPCR quantitation of the indicated transcripts upon ASO treatment as in panel (A). All tested transcripts were normalized to the *HPRT* transcript level. Relative expression to the NTC is presented. (D) Western blotting analysis of the PKM isoform switch after ASO treatment as in panel (A). The bar charts in panel (B and C) represent the average of three independent biological replicates ± SEM. One-way ANOVA was performed with Dunnett's multiple comparison post-hoc test. ** $P \leq 0.01$; *** $P \leq 0.001$.

Figure 2. Delivery of ASO1-cEt/DNA by free uptake induces *PKM* splice switching in Huh7 cells

(A) ASO1-cEt/DNA induces *PKM* splice switching in a dose-dependent manner. Radioactive RT-PCR analysis after treating Huh7 cells with varying ASO concentrations by free uptake for four days. (B) Quantification of PKM1 and PKMds isoforms in panel (A). (C) Radioactive RT-PCR analysis after treating Huh7 cells with 20 μM ASO by free uptake for seven days. Medium and ASO were replenished on day 4. (D) Quantification of PKM1 and PKMds isoforms in panel (C). (E) Western blotting analysis of the PKM isoform switch after treating Huh7 cells with ASO as in panel (C). The bar charts in panels (B and D) represent the average of three independent biological replicates ± SEM. One-way ANOVA was performed with Dunnett's multiple comparison post-hoc test. * $P \leq 0.05$; ** $P \leq 0.01$; *** $P \leq 0.001$.

Figure 3. ASO1-cEt/DNA inhibits Huh7 cell growth *in vitro*

(A) ASO1-cEt/DNA slows down growth of Huh7 cells. Cells were counted with a hemocytometer. Huh7 cells were treated with 20 μM ASO by free uptake for the indicated time points. (B) ASO1-cEt/DNA induces apoptosis. Annexin V staining was done on day 5 after treating Huh7 cells with 20 μM ASO by free uptake for four days. Cells were stained with Annexin V (green) and Hoechst (blue). Scale bar = 200 μm. (C) Quantification of Annexin V-positive cells in panel (B) was done by dividing the total number of cells (N>300). (D) ASO1-cEt/DNA inhibits cell proliferation. EdU staining was performed after treating Huh7 cells with 20 μM ASO as in panel (B). Cells were stained with EdU (red) and DAPI (blue). Scale bar = 200 μm. (E) Quantification of EdU-positive cells in panel (D) was done by dividing the total number of cells (N>300). All data in panels (A, C, and E) represent the average of three independent biological replicates ± SEM. One-way ANOVA was performed with Dunnett's multiple comparison post-hoc test. * $P \leq 0.05$; ** $P \leq 0.01$; *** $P \leq 0.001$.

Figure 4. ASO1-cEt/DNA-dependent slow-growth phenotype is an on-target effect

(A) Cells were counted with a hemocytometer. Huh7 cells expressing T7-PKM2 or luciferase-strawberry were treated with 20 μM ASO by free uptake for the indicated times. (B) Quantification of Annexin V-positive Huh7 cells expressing T7-PKM2 or luciferase-strawberry in separate stable cell lines, following treatment with 20 μM ASO by free uptake for four days. (C) Quantification of EdU-positive Huh7 cells expressing T7-PKM2 or luciferase-strawberry in separate stable cell lines, following treatment with 20 μM ASO as in panel (B). All data represent the average of three independent biological replicates ± SEM. One-way ANOVA was performed with Dunnett's multiple comparison post-hoc test. * $P \leq 0.05$; ** $P \leq 0.01$; *** $P \leq 0.001$.

Figure 5. ASO1-cEt/DNA stimulates pyruvate kinase activity and alters glucose metabolism

(A) Pyruvate kinase activity increases upon ASO1-cEt/DNA treatment. Pyruvate kinase assay was performed after treating Huh7 cells with 20 μM ASO by free uptake for four days. Pyruvate kinase (PK) activity was normalized to 5×10^4 cells. The bar chart represents the average of three independent biological replicates ± SEM. (B) ASO1-cEt/DNA alters glucose metabolism. Huh7 cells were treated with 20 μM ASO by free uptake for seven days. Medium and ASO were replenished on day 4. LC-MS was conducted on extracted metabolites after incubating Huh7 cells in medium with [U-^{13}C]-glucose for 8 hrs on day 7. Data are the average of five independent cultures ± SEM. One-way ANOVA was performed with Dunnett's multiple comparison post-hoc test in panel (A), and with Tukey's multiple comparison post-hoc test in panel (B). * $P \leq 0.05$; ** $P \leq 0.01$; *** $P \leq 0.001$.

Figure 6. ASO1-cEt/DNA inhibits HepG2 cell growth in a xenograft model

(A) Schematic of ASO dosing schedule in the HepG2 xenograft mouse model. 2×10^6 HepG2 cells) were transplanted on day 0 and allowed to grow for 10 days prior to the first ASO treatment. ASOs (250 mg/kg/wk) were delivered subcutaneously with a weekly schedule of five consecutive-day injections, followed by two days without injection, for three weeks. (B) Whole-animal live imaging of mice with luciferase-integrated HepG2 cells that were orthotopically transplanted in the liver. Luminescence images of transplanted mice on day 3 and day 29 are shown with a color scale from 2×10^7 (min) – 5×10^9 (max). A total of 18 mice (N=18) were randomized to each treatment group; one saline-treated mouse died on day 18. (C) Quantification of luciferase signal in panel (B). The average of five or six biological replicates ± SEM is shown. (D) Representative pictures of tumors on day 29. Scale bar = 5 mm. (E) Quantification of tumor volume on day 29. (F) Representative IHC images of Ki67 expression in liver sections with tumors on day 29. Scale bar indicates 50 μm. (G) Quantification of Ki67-positive cells in panel (F). (H) Representative pictures of immunohistochemistry analysis of ASO localization in liver sections with tumors on day 29. Rabbit anti-ASO antibody recognizes the phosphorothioate backbone. H&E staining of the corresponding sections are shown. Scale bar = 250 μm for 4× and

25 μm for 40×. (I) ASO1-cEt/DNA induces *PKM* splice switching in a HepG2 xenograft model. Radioactive RT-PCR was performed on liver-tumor samples removed from the transplanted mice on day 29. Quantification of PKM1 and PKMds isoforms is shown. (J) Western blotting analysis of PKM isoform switch in HepG2 xenografts. Protein lysates were extracted from liver-tumor samples removed from the transplanted mice on day 29. Quantification of PKM1 and PKM2 isoforms is shown. Data in panels (E, G, I, and J) are the average of three biological replicates ± SEM. One-way ANOVA was performed with Dunnett's multiple comparison post-hoc test. * $P \leq 0.05$; ** $P \leq 0.01$; *** $P \leq 0.001$.

Figure 7. mASO3-cEt/DNA inhibits tumor growth in a HCC genetic mouse model

(A) Schematic of ASO dosing schedule in the genetic mouse model. Liver tumors were induced by introducing Sleeping Beauty transposase and c-myc plasmids via hydrodynamic tail-vein injection on day 0. Liver tumors were allowed to grow for 28 days prior to the first mouse-specific ASO (mASO) treatment. mASOs (250 mg/kg/wk) were delivered subcutaneously with a weekly schedule of five-consecutive day injections, followed by two days without injections, for three weeks. (B) Measurements of tumor weight normalized to the weight of the whole liver, in different treatment groups on day 47. A total of 60 mice (N=60) were randomized to each treatment group, which includes 10 male (blue dots) and 10 female (red dots) mice. The average of 20 biological replicates ± SEM is shown. (C) Representative pictures of livers with tumors on day 47. Scale bar = 5 mm. (D) mASO3-cEt/DNA induces *mPKM* splice switching in liver tumors, as shown in the representative autoradiograph. Radioactive RT-PCR was performed on liver-tumor samples from tumor-bearing mice on day 47. (E) Quantification of mPKM1 and mPKMds isoforms in panel (D). The bar chart is the average of three biological replicates ± SEM. (F) mASO3-cEt/DNA extends the survival of liver-tumor-bearing mice. Mice (N=42) were randomized in each treatment group, which includes 7 male and 7 female mice. Log-rank test was performed with Bonferroni-corrected threshold ($P = 0.0166$). Saline-treated mice (black) had a median survival of 45 days; Ctrl-cEt/DNA-treated mice (green) had a median survival of 45.5 days ($P = 0.9240$); and mASO3-cEt/DNA-treated mice (orange) had a median survival of 61.5 days ($P = 0.0001$). (G) mASO3-cEt/DNA had no observable toxicity in wild-type mice. Histological slides of the indicated organs from saline-treated or mASO3-cEt/DNA-treated mice. Scale bar = 100 μm. One-way ANOVA was performed with Dunnett's multiple comparison post-hoc test in panel (B and E). * $P \leq 0.05$; *** $P \leq 0.001$.

Supplementary Figure 1. PKM2 is the predominant isoform in HCC cells, and ASO1-cEt/DNA induces *PKM* splice switching in HepG2 cells

(A) RT-qPCR analysis of *PKLR* and *PKM2* transcript levels in different HCC cell lines and normal human liver. All tested transcripts were normalized to *HPRT* transcript level. Relative expression to normal liver is presented. (B) Radioactive RT-PCR analysis shows the degree of *PKM* splice switching after transfecting HepG2 cells with 60 nM ASO for two days. (C) Quantification of PKM1 and PKMds isoforms in panel (B). (D) RT-qPCR shows transcript levels

after ASO treatment as in panel (B). All tested transcripts were normalized to *HPRT*, And relative expression to NTC is presented. (E) Western blotting analysis of PKM isoform switch. Protein lysates were prepared after ASO treatment as in panel (B). (F) ASO1-cEt/DNA induces *PKM* splice switching in a dose-dependent manner. Radioactive RT-PCR analysis of HepG2 cells treated with varying concentrations of ASO by free uptake for four days. (G) Quantification of PKM1 and PKMds isoforms in panel (F). (H) Radioactive RT-PCR analysis of RNA from HepG2 cells incubated with 20 μM ASO by free uptake for seven days. Medium and ASO were replenished on day 4. (I) Quantification of PKM1 and PKMds isoforms in panel (H). (J) Western blotting analysis of PKM isoform switch, after treating HepG2 cells with 20 μM ASO as in panel (H). The bar charts in panels (A, C, D, G, and I) represent the average of three independent biological replicates ± SEM. One-way ANOVA was performed with Dunnett's multiple comparison post-hoc test. * $P \leq 0.05$; ** $P \leq 0.01$; *** $P \leq 0.001$.

Supplementary Figure 2. ASO1-cEt/DNA inhibits HepG2 cell growth *in vitro*

(A) ASO1-cEt/DNA is toxic to HCC cells. Representative images of HepG2 (left) and Huh7 (right) cells following NTC, Ctrl-cEt/DNA, or ASO1-cEt/DNA treatment. Scale bar = 200 μm. (B) ASO1-cEt/DNA slows down growth of HepG2 cells. Cells were counted with a hemocytometer. HepG2 cells were treated with 20 μM ASO by free uptake for the indicated times. (C) ASO1-cEt/DNA induces apoptosis. Annexin V staining was done on day 5 after treating HepG2 cells with 20 μM ASO by free uptake for four days. Cells were stained with Annexin V (green) and Hoechst (blue). Scale bar = 200 μm. (D) Quantification of Annexin V-positive cells in panel (C) was done by dividing the total number of cells (N>300). (E) ASO1-cEt/DNA inhibits cell proliferation. EdU staining was performed after treating HepG2 cells with 20 μM ASO as in panel (C). Cells were stained with EdU (red) and DAPI (blue). Scale bar = 200 μm. (F) Quantification of EdU-positive cells in panel (E) was done by dividing the total number of cells (N>300). All data in panels (B, D, and F) represent the average of three independent biological replicates ± SEM. One-way ANOVA was performed with Dunnett's multiple comparison post-hoc test. ** $P \leq 0.01$; *** $P \leq 0.001$.

Supplementary Figure 3. Enforced expression of individual PKM isoforms

(A) Schematic diagram of different T7-tag PKM isoforms and luciferase-strawberry cDNAs that were individually cloned into a lentiviral expression vector, which carries a puromycin-selection marker. (B) Various T7-tag PKM isoforms were successfully expressed in HepG2 (top) and Huh7 (bottom) cells, as detected by Western blotting. Numbers below the blots indicate the fold change relative to cells expressing luciferase-strawberry; # indicates a non-specific band. (C) T7-PKM1 and T7-PKM2 isoforms are catalytically active. Pyruvate kinase assays were performed in cell lysates incubated with or without 5 mM FBP for 30 min at room temperature. Pyruvate kinase activity was normalized to 5×10^4 cells. All data in panel (C) represent the average of three independent biological replicates ± SEM. One-way ANOVA was performed with Tukey's multiple comparison post-hoc test. * $P \leq 0.05$; ** $P \leq 0.01$; *** $P \leq 0.001$.

Supplementary Figure 4. ASO1-cEt/DNA-dependent slow-growth phenotype is an on-target effect, and enforced expression of PKM1 is sufficient to inhibit HCC cell growth

(A) Enforced expression of PKM2 partially rescues the ASO1-cEt/DNA-dependent slow-growth phenotype. Cells were counted with a hemocytometer. HepG2 cells expressing T7-PKM2 or luciferase-strawberry were treated with 20 μM ASO by free uptake for the indicated times. (B) Quantification of Annexin V-positive HepG2 cells expressing T7-PKM2 or luciferase-strawberry treated with 20 μM ASO by free uptake for four days. (C) Quantification of EdU-positive HepG2 cells expressing T7-PKM2 or luciferase-strawberry treated with 20 μM ASO as in panel (B). (D) Soft-agar assay was performed in HepG2 cells expressing luciferase-strawberry or T7-PKM1. 10,000 HepG2 cells/well were plated with soft agar and incubated at 37 °C/5% CO_2 for 2 months. (E) Quantification of the number of colonies in panel (D). (F) Soft-agar assay with Huh7 cells expressing luciferase-strawberry or T7-PKM1. 50,000 Huh7 cells/well were plated with soft agar and incubated at 37 °C/5% CO_2 for 3 weeks. (G) Quantification of the number of colonies in panel (F). All data in panels (A – C, E, and G) represent the average of three independent biological replicates ± SEM. One-way ANOVA was performed with Dunnett's multiple comparison post-hoc test. * $P \leq 0.05$; ** $P \leq 0.01$; *** $P \leq 0.001$.

Supplementary Figure 5. ASO1-cEt/DNA increases pyruvate kinase activity and decreases lactate secretion in HCC cells

(A) Pyruvate kinase activity in HepG2 cells increased upon ASO1-cEt/DNA treatment. Pyruvate kinase assay was performed after treating HepG2 cells with 20 μM ASO by free uptake for four days. Pyruvate kinase (PK) activity was normalized to 5×10^4 cells. The bar chart represents the average of three independent biological replicates ± SEM. (B) Levels of lactate released to the medium were measured in Huh7 cells treated with 20 μM ASO by free uptake for seven days. The medium and ASO were replenished on day 4. LC-MS was conducted on extracted metabolites from the medium after incubating Huh7 cells in medium with [U-^{13}C] glucose for 8 hours on day 7. The levels of lactate release were normalized to the number of cells. Data are the average of five independent cultures ± SEM. One-way ANOVA was performed with Dunnett's multiple comparison post-hoc test in panel (A) and with Tukey's multiple comparison post-hoc test in panel (B). *** $P \leq 0.001$.

Supplementary Figure 6. ASO1-cEt/DNA is more potent than ASO2-cEt/DNA in inhibiting HepG2 growth in a xenograft model, and enforced expression of PKM1 is sufficient to inhibit HCC cell growth *in vivo*

(A) Schematic diagram of ASO1-cEt/DNA and ASO2-cEt/DNA targeted regions. ASO1-cEt/DNA targets a region we previously identified (30, red region), whereas ASO2-cEt/DNA targets an SRSF3 binding site (blue region, (30)). (B) ASO1-cEt/DNA has higher potency than ASO2-cEt/DNA to switch *PKM* switching in HepG2 cells. Radioactive RT-PCR analysis of RNA

from HepG2 cells transfected with 60 nM ASO. (C) Quantification of PKM1 and PKMds isoforms in panel (B). (D) Whole-animal live imaging of mice with luciferase-integrated HepG2 cells that were orthotopically transplanted in the liver. Luminescence images of transplanted mice on day 3 and day 29 are shown, with color scale from 2×10^7 (min) – 5×10^9 (max). Mice (N=24) were randomized to each treatment group; one saline-treated mouse died on day 18. (E) Quantification of luciferase signal in panel (D). The average of five or six biological replicates ± SEM is shown. (F) Representative pictures of tumors on day 29. Scale bar = 5 mm. (G) Quantification of tumor volume on day 29. (H) Representative IHC images of Ki67 expression in liver sections with tumors on day 29. Scale bar = 50 μm. (I) Quantification of Ki67-positive cells in panel (H). (J) Enforced expression of PKM1 is sufficient to inhibit HepG2 cell growth *in vivo*. Representative pictures of tumors on day 29. Scale bar = 5 mm. (K) Quantification of tumor volume in panel (J). All data in panels (C, G, I, and K) are the average of three biological replicates ± SEM. One-way ANOVA was performed with Dunnett's multiple comparison post-hoc test. * $P \leq 0.05$; ** $P \leq 0.01$; *** $P \leq 0.001$.

Supplementary Figure 7. GN3 conjugation does not enhance the potency of mASO3-cEt/DNA in a HCC genetic mouse model

(A) mASO3-cEt/DNA induces *mPKM* splice-switching in HepA1-6 cells. Radioactive RT-PCR analysis of HepA1-6 cells transfected with 60 nM ASO. (B) Quantification of PKM1 and PKMds isoforms in panel (A). (C) Western blotting analysis of mPKM isoforms. # indicates a non-specific band. (D) No significant enhancement of mASO3-cEt/DNA potency by GN3 conjugation. Mice (N=80) were randomized to each treatment group, which includes 10 male (blue dots) and 10 female (red dots) mice. The average of 20 biological replicates ± SEM is shown. One-way ANOVA was performed with Dunnett's multiple comparison post-hoc test. ** $P \leq 0.01$; *** $P \leq 0.001$. (E) Representative images of livers with tumors on day 47. Scale bar = 5 mm. (F) ASGPR1 is down-regulated in liver tumor. Western blotting analysis of protein lysate from a liver tumor (T) or the adjacent normal liver tissue (Adj) on Day 47.

Figure 1

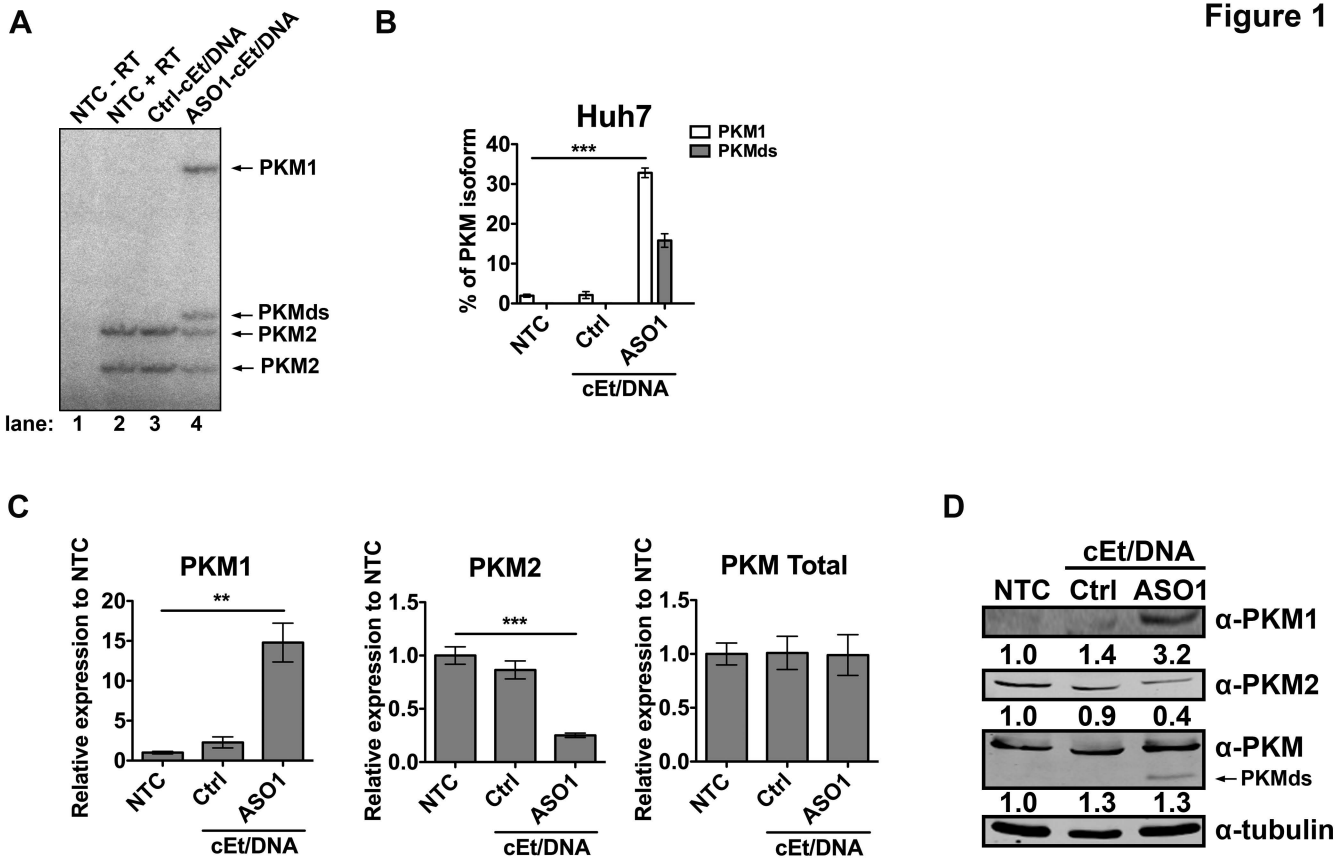
A
NTC - RT
NTC + RT
Ctrl-cEt/DNA
ASO1-cEt/DNA
PKM1
PKMds
PKM2
PKM2
lane: 1 2 3 4
B
Huh7
PKM1
PKMds
% of PKM isoform
***
NTC
Ctrl
ASO1
cEt/DNA
C
PKM1
**
Relative expression to NTC
NTC
Ctrl
ASO1
cEt/DNA
PKM2
***
PKM Total
D
cEt/DNA
NTC
Ctrl
ASO1
α-PKM1
1.0 1.4 3.2
α-PKM2
1.0 0.9 0.4
α-PKM
PKMds
1.0 1.3 1.3
α-tubulin

Figure 2

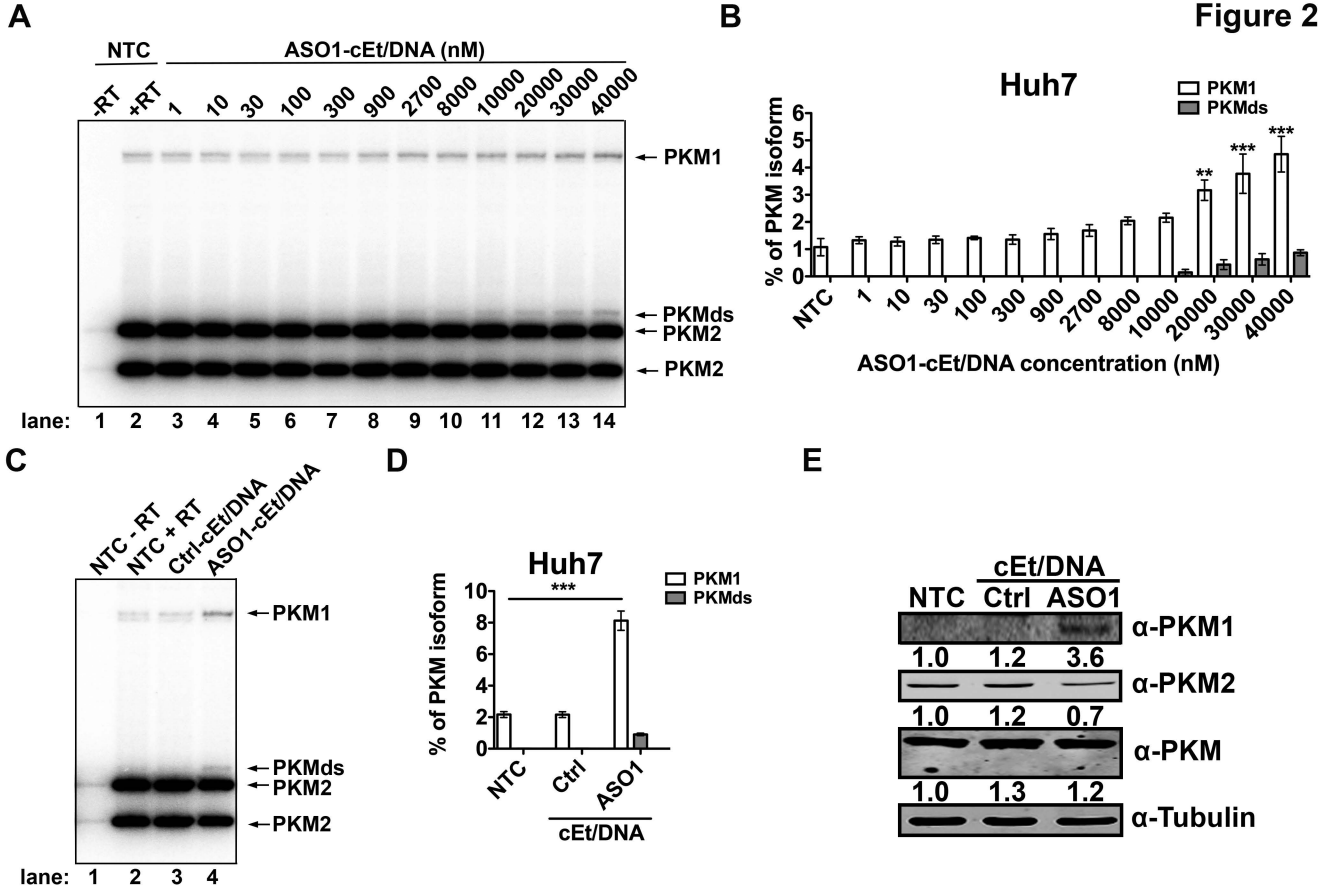
A
NTC
ASO1-cEt/DNA (nM)
-RT
+RT
1
10
30
100
300
900
2700
8000
10000
20000
30000
40000
PKM1
PKMds
PKM2
PKM2
lane: 1 2 3 4 5 6 7 8 9 10 11 12 13 14
B
Huh7
PKM1
PKMds
% of PKM isoform
**
***
***
NTC
1
10
30
100
300
900
2700
8000
10000
20000
30000
40000
ASO1-cEt/DNA concentration (nM)
C
NTC - RT
NTC + RT
Ctrl-cEt/DNA
ASO1-cEt/DNA
PKM1
PKMds
PKM2
PKM2
lane: 1 2 3 4
D
Huh7
PKM1
PKMds
% of PKM isoform
***
NTC
Ctrl
ASO1
cEt/DNA
E
cEt/DNA
NTC
Ctrl
ASO1
α-PKM1
1.0 1.2 3.6
α-PKM2
1.0 1.2 0.7
α-PKM
1.0 1.3 1.2
α-Tubulin

A

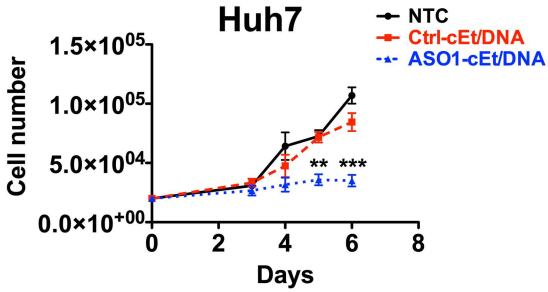
Huh7
NTC
Ctrl-cEt/DNA
ASO1-cEt/DNA
Cell number
1.5×10^05
1.0×10^05
5.0×10^04
0.0×10^+00
0
2
4
6
8
Days
**
***

B

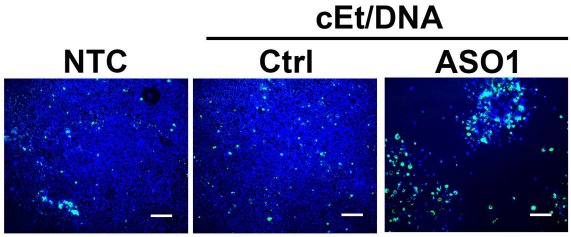
cEt/DNA
NTC
Ctrl
ASO1

C

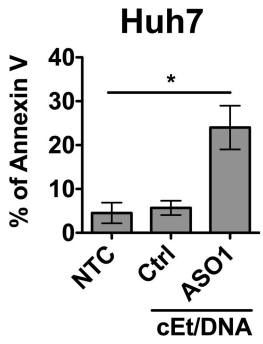
Huh7
% of Annexin V
40
30
20
10
0
*
NTC
Ctrl
ASO1
cEt/DNA

D

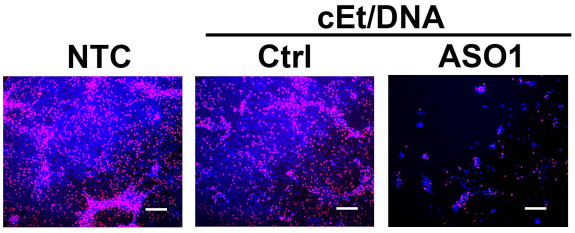
cEt/DNA
NTC
Ctrl
ASO1

E

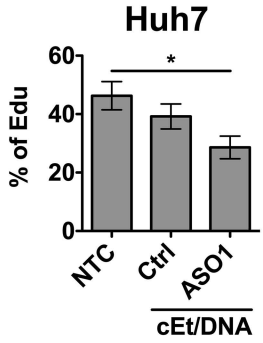
Huh7
% of Edu
60
40
20
0
*
NTC
Ctrl
ASO1
cEt/DNA

Figure 4

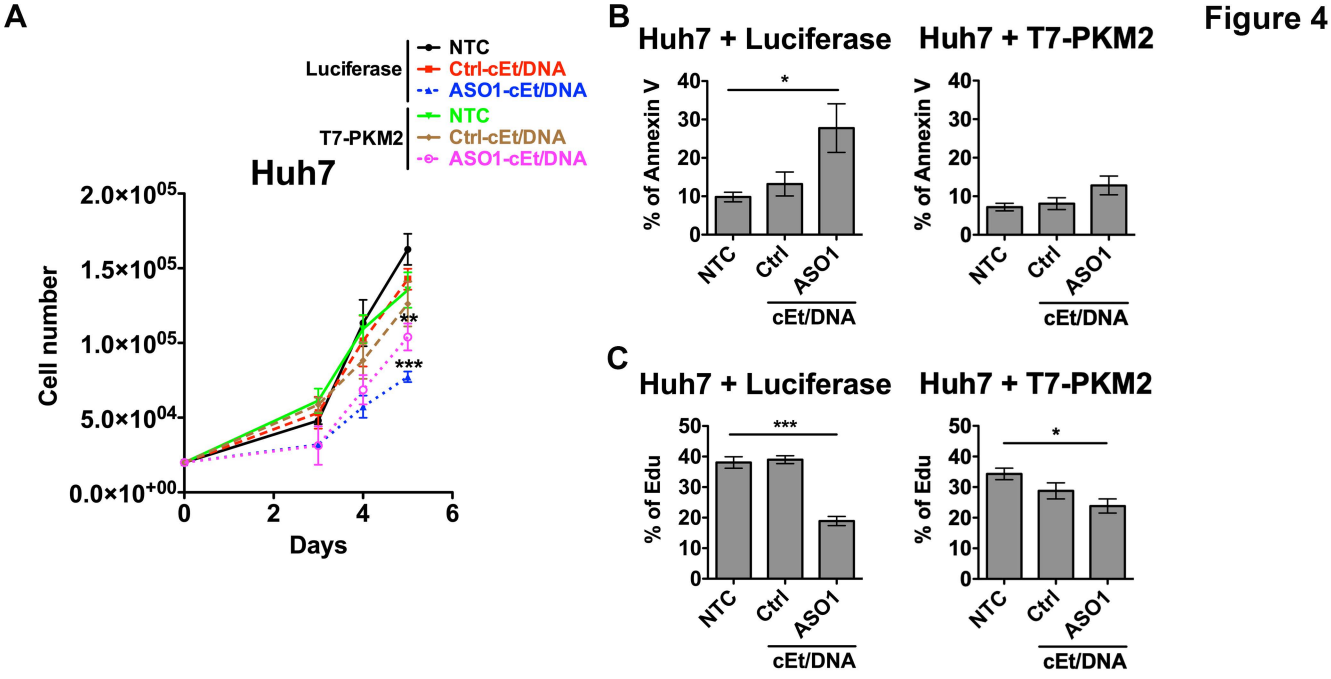
A
Luciferase
NTC
Ctrl-cEt/DNA
ASO1-cEt/DNA
T7-PKM2
NTC
Ctrl-cEt/DNA
ASO1-cEt/DNA
Huh7
Cell number
2.0×10^05
1.5×10^05
1.0×10^05
5.0×10^04
0.0×10^+00
0
2
4
6
Days
**
***
B
Huh7 + Luciferase
Huh7 + T7-PKM2
% of Annexin V
40
30
20
10
0
*
NTC
Ctrl
ASO1
cEt/DNA
C
Huh7 + Luciferase
Huh7 + T7-PKM2
% of Edu
50
40
30
20
10
0
***
*
NTC
Ctrl
ASO1
cEt/DNA

A

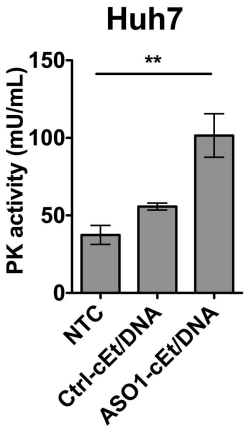
Huh7
PK activity (mU/mL)
150
100
50
0
**
NTC
Ctrl-cEt/DNA
ASO1-cEt/DNA

B

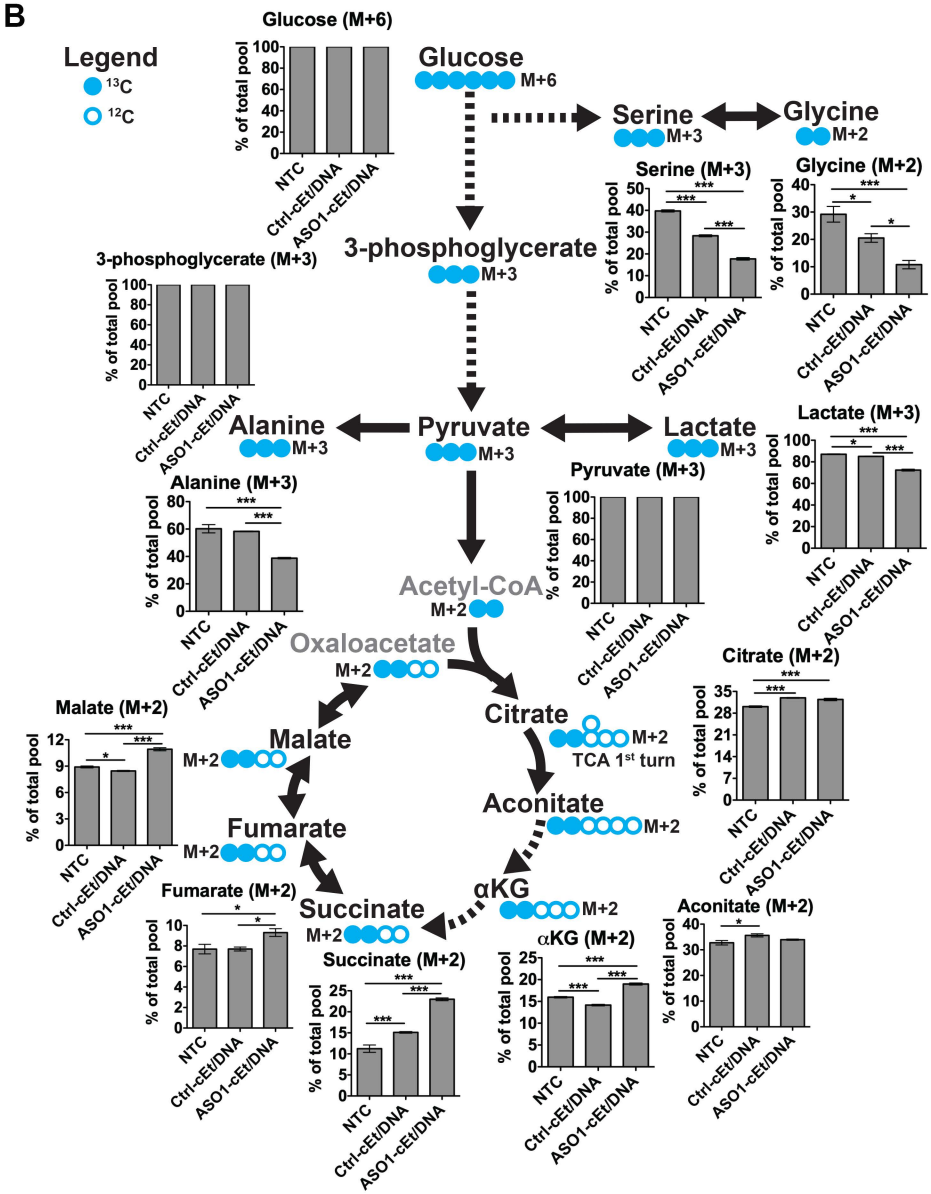
Legend
13C
12C
Glucose (M+6)
Glucose
M+6
Serine
M+3
Glycine
M+2
Serine (M+3)
Glycine (M+2)
3-phosphoglycerate
M+3
3-phosphoglycerate (M+3)
Alanine
M+3
Pyruvate
M+3
Lactate
M+3
Alanine (M+3)
Pyruvate (M+3)
Lactate (M+3)
Acetyl-CoA
M+2
Oxaloacetate
M+2
Citrate
M+2
TCA 1st turn
Citrate (M+2)
Malate
M+2
Malate (M+2)
Aconitate
M+2
Aconitate (M+2)
Fumarate
M+2
Fumarate (M+2)
αKG
M+2
αKG (M+2)
Succinate
M+2
Succinate (M+2)
% of total pool
NTC
Ctrl-cEt/DNA
ASO1-cEt/DNA

Figure 6

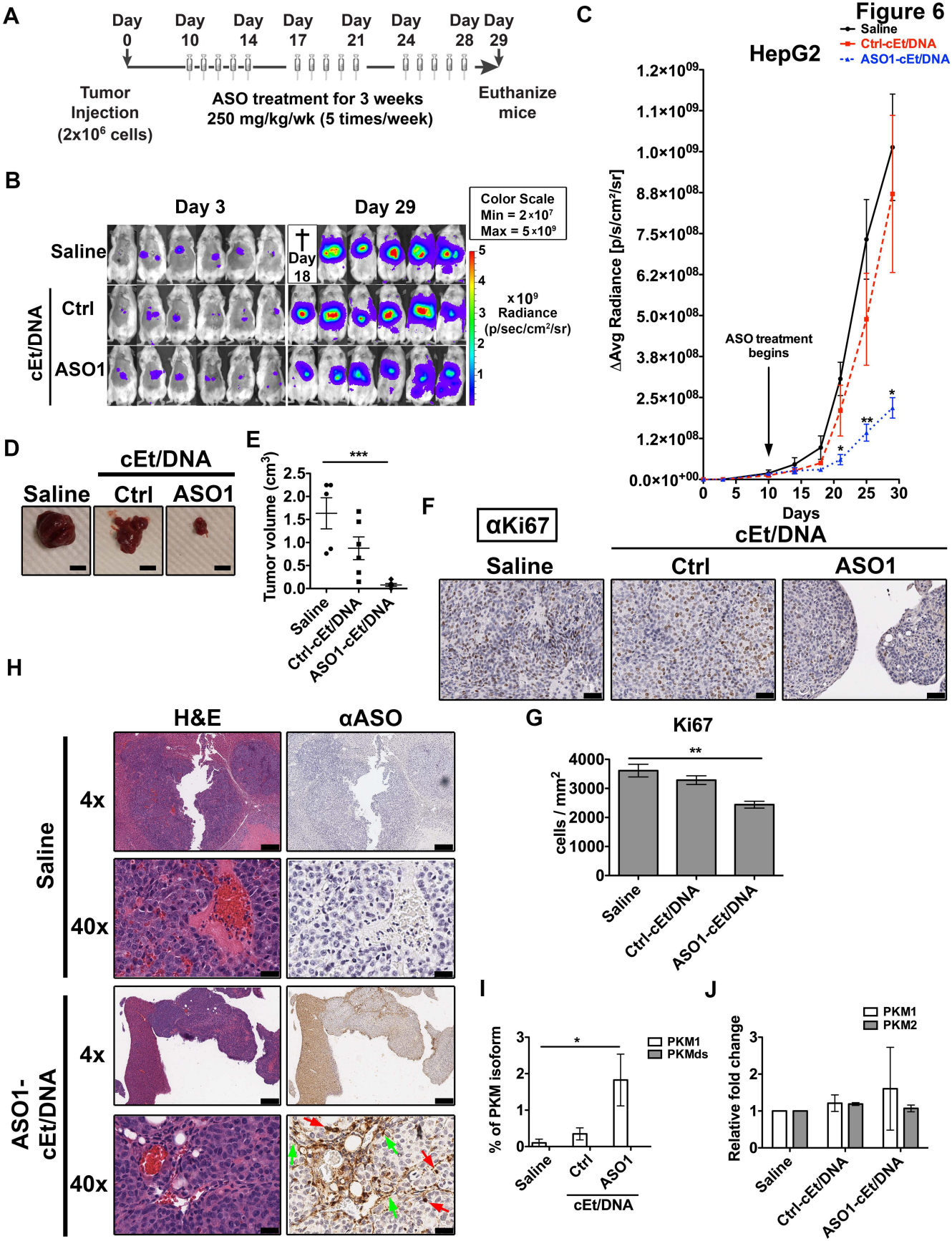
A
Day 0
Day 10
Day 14
Day 17
Day 21
Day 24
Day 28
Day 29
Tumor Injection (2x10^6 cells)
ASO treatment for 3 weeks 250 mg/kg/wk (5 times/week)
Euthanize mice
B
Day 3
Day 29
Color Scale Min = 2×10^7 Max = 5×10^9
Saline
Ctrl
ASO1
cEt/DNA
Day 18
x10^9 Radiance (p/sec/cm²/sr)
C
HepG2
Saline
Ctrl-cEt/DNA
ASO1-cEt/DNA
ΔAvg Radiance [p/s/cm²/sr]
ASO treatment begins
Days
D
cEt/DNA
Saline
Ctrl
ASO1
E
Tumor volume (cm³)
***
Saline
Ctrl-cEt/DNA
ASO1-cEt/DNA
F
αKi67
cEt/DNA
Saline
Ctrl
ASO1
G
Ki67
cells / mm²
**
Saline
Ctrl-cEt/DNA
ASO1-cEt/DNA
H
H&E
αASO
Saline
4x
40x
ASO1-cEt/DNA
4x
40x
I
% of PKM isoform
*
PKM1
PKMds
Saline
Ctrl
ASO1
cEt/DNA
J
PKM1
PKM2
Relative fold change
Saline
Ctrl-cEt/DNA
ASO1-cEt/DNA

Figure 7

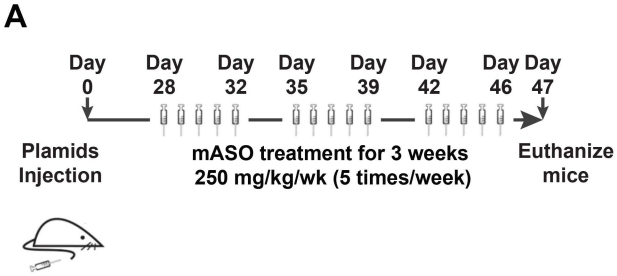
A
Day 0
Day 28
Day 32
Day 35
Day 39
Day 42
Day 46
Day 47
Plamids Injection
mASO treatment for 3 weeks
250 mg/kg/wk (5 times/week)
Euthanize mice

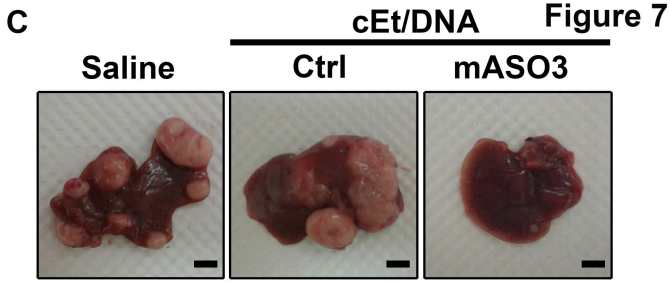
C
cEt/DNA
Saline
Ctrl
mASO3

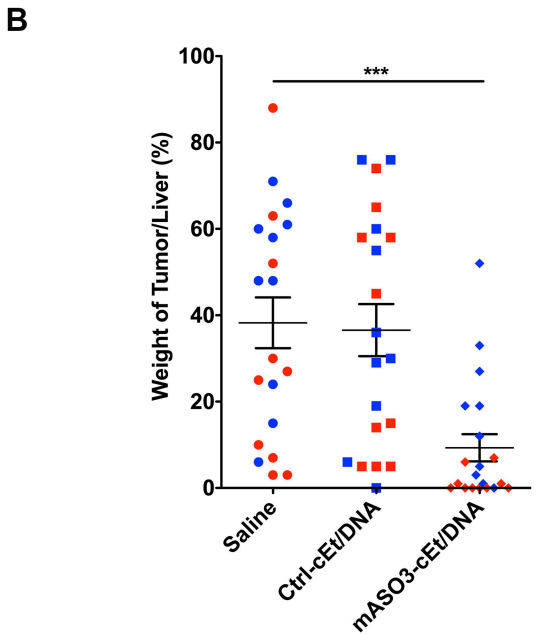
B
Weight of Tumor/Liver (%)
***
Saline
Ctrl-cEt/DNA
mASO3-cEt/DNA

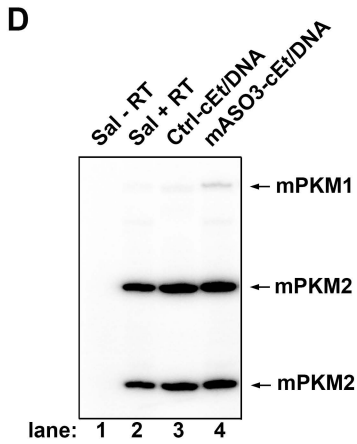
D
Sal - RT
Sal + RT
Ctrl-cEt/DNA
mASO3-cEt/DNA
mPKM1
mPKM2
mPKM2
lane: 1 2 3 4

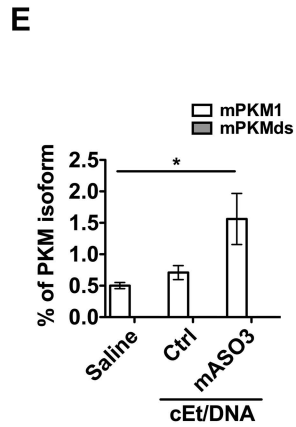
E
mPKM1
mPKMds
% of PKM isoform
*
Saline
Ctrl
mASO3
cEt/DNA

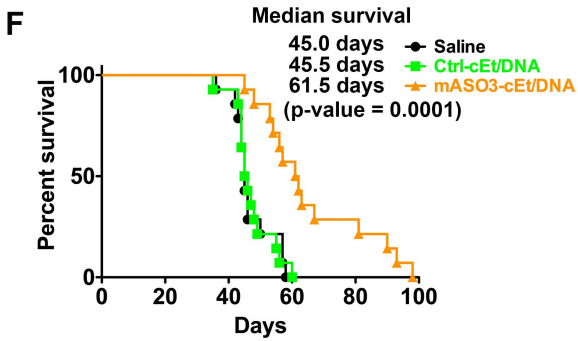
F
Median survival
45.0 days
45.5 days
61.5 days
(p-value = 0.0001)
Saline
Ctrl-cEt/DNA
mASO3-cEt/DNA
Percent survival
Days

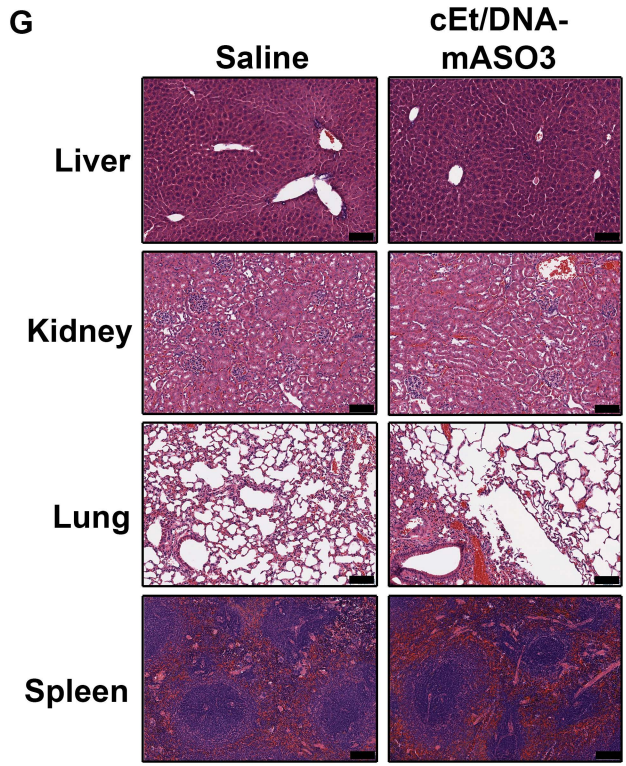
G
Saline
cEt/DNA-mASO3
Liver
Kidney
Lung
Spleen